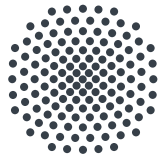


BACHELOR THESIS

---

**Setting up an optical accordion lattice  
to determine the resolution of a  
Rydberg ion imaging system**

---



**University of Stuttgart**  
5th Institute of Physics

Luca Schmidt  
9th August 2018

Examiner: Prof. Dr. Tilman Pfau

University of Stuttgart  
5. Physikalisches Institut  
Pfaffenwaldring 57, DE-70569 Stuttgart



# Declaration

I hereby declare that this submission is my own work and that, to the best of my knowledge and belief, it contains no material previously published or written by another person, except where due acknowledgment has been made in the text.

Luca Schmidt

Stuttgart, 9th August 2018



# Abstract

## 1. Deutsch

In der vorliegenden Bachelorarbeit wird ein experimenteller Aufbau zur Erzeugung eines optischen Gitters mit variabler Gitterkonstante vorgestellt. Dieser soll dazu dienen, eine Wolke ultrakalter Atome in einem wohldefinierten räumlichen Muster zu ionisieren, und damit die Kalibration eines Rydberg-Ionenmikroskops ermöglichen. Desweiteren soll mithilfe des variablen Testmusters das Auflösungsvermögen des Ionenmikroskops bestimmt werden.

Die Arbeit umfasst sowohl ein maßgefertigtes Design des Aufbaus zum Einbau in das bestehende Rydberg-Experiment, als auch die Charakterisierung des erzeugten optischen Akkordeon-Gitters. Neben der Bestimmung der Grenzen für die veränderbare Gitterkonstante wird eine Analyse des Gitters in Bezug auf Sichtfeld und Tiefenschärfe durchgeführt.

Ein besonderer Schwerpunkt liegt auf der Untersuchung der thermischen Stabilität des Aufbaus.

## 2. English

The bachelor thesis at hand reports on an experimental setup to create an optical lattice with a variable lattice period. It shall be used to ionise an ultracold atomic cloud in a well-defined spatial pattern and thereby serve to calibrate a Rydberg ion microscope and to test the microscope's resolution.

This work includes a customised setup design in order to integrate it into the existing experimental architecture. Furthermore, it provides a characterisation of the created optical accordion lattice in terms of the achievable range of the lattice period, the field of view and the depth of field.

A special focus is laid on the thermal stability of the setup.



# Contents

<b>Declaration</b>	<b>iii</b>
<b>Abstract</b>	<b>v</b>
1. Deutsch . . . . .	v
2. English . . . . .	v
<b>List of abbreviations</b>	<b>ix</b>
<b>1. Introduction</b>	<b>1</b>
<b>2. Theory</b>	<b>4</b>
2.1. Laser . . . . .	4
2.1.1. Working principle . . . . .	4
2.1.2. Diode laser . . . . .	5
2.2. Geometrical optics . . . . .	7
2.2.1. ABCD-matrix formalism . . . . .	7
2.2.2. Lens systems . . . . .	8
2.2.3. Spherical aberrations . . . . .	10
2.3. Polarising optical elements . . . . .	11
2.4. Gaussian optics . . . . .	12
2.5. Accordion lattice . . . . .	14
2.5.1. Interference of two wavefronts . . . . .	14
2.5.2. Lattice period . . . . .	15
2.5.3. Visibility . . . . .	16
2.6. Thermal expansion . . . . .	16
<b>3. Experimental setup</b>	<b>17</b>
3.1. Schematic setup . . . . .	17
3.2. Experimental requirements . . . . .	19
3.3. Realisation of the titanium setup mount . . . . .	19
<b>4. Results</b>	<b>23</b>
4.1. Simulations . . . . .	23
4.1.1. Transverse diameter of the optical lattice . . . . .	23

4.1.2.	Focal shift between centre and off-centre beams . . . . .	24
4.2.	Characterisation of the Raspberry Pi camera . . . . .	25
4.3.	Lattice characterisation . . . . .	26
4.3.1.	Variation of lattice period . . . . .	26
4.3.2.	Field of view . . . . .	28
4.3.3.	Depth of field . . . . .	31
4.3.4.	Thermal stability . . . . .	33
<b>5.</b>	<b>Summary</b>	<b>37</b>
<b>6.</b>	<b>Outlook</b>	<b>39</b>
	<b>Appendix</b>	<b>41</b>
A.	Technical drawings . . . . .	41
	<b>List of Figures</b>	<b>49</b>
	<b>Bibliography</b>	<b>50</b>

# List of abbreviations

**E-field** Electric field

**laser** Light amplification by stimulated emission of radiation

**MOT** Magneto-optical trap

**PBS** Polarising beam splitter

**PID** Proportional-integral-derivative

**VSCPT** Velocity selective coherent population trapping



# 1. Introduction

At the turn of the twentieth century, physicists had gathered rough knowledge about the internal structure of atoms which mainly resulted from the analysis of the spectral lines of the sun and individual elements. It was known by then, that an atom consists of a dilute shell of one or more electrons that surrounds a single dense nucleus with positive charge. With the advent of quantum mechanics in the first few decades of the century, it became possible to explain the existing experimental data with a profound mathematical theory that described the electrons as matter waves with the energy quantisation resulting from the constructive interference requirement. The new description delivered increasingly accurate predictions about both the atomic energy levels and their behaviour when the atom is interacting with external electric or magnetic fields, electromagnetic radiation or other atoms. Soon, there was the necessity to built advanced experimental setups to verify these predictions. It turned out to be advantageous to study atoms in ultracold assembles where the measured quantities were no longer obscured by the thermal motion of hot atoms. Obtaining and controlling such ultracold atomic gases required both advanced cooling techniques and elaborate atomic traps. Great steps in the pursuit of atomic cooling were made by the development of laser cooling [1], Doppler and sub-Doppler cooling [2] in the second half of the twentieth century. These techniques made it possible to reach temperatures of a view hundred nanokelvin. Even lower temperatures were realised by the so-called ‘sub-recoil’ cooling via evaporation [3] or VSCPT<sup>1</sup> [4, 5], which enabled temperatures in the region of a view nanokelvin. In terms of trapping, the development of dipolar traps and magneto-optical traps (MOT) paved the way for many of the modern atomic physics experiments [6].

Today, one active field of research within atomic physics is Rydberg physics. It is concerned with atoms that have at least one electron excited to a high energy level. Rydberg atoms feature exaggerated properties compared to ground state atoms such as their extraordinary size, lifetime and susceptibility to external fields [7, 8]. These exceptional properties lay at the heart of interesting phenomena observed with Rydberg atoms, such as the formation of a novel type of molecules [9, 10] or the occurrence of a so-called Rydberg blockade which is a certain volume around a first highly excited atom where no other Rydberg excitation is possible due to the strong Rydberg-Rydberg interaction that shifts the other Rydberg state out of resonance [11, 12]. This blockade mechanism can mediate interactions between single photons which opens the door for quantum nonlinear optics in a single photon regime [13]. Additionally, it allows the simulation of quantum magnetism models, e.g. the Ising models, from the field of condensed-matter physics [14, 15]. A remarkable step, which makes Rydberg atoms promising objects for quantum information science,

---

<sup>1</sup>Velocity selective coherent population trapping

was the creation of entangled states with the help of the Rydberg blockade [16, 17].

Large lengthscales in the range of a few micrometers make Rydberg physics suitable for spatially resolved investigations. Several experiments that aim on spatial resolution of Rydberg atoms were taken into operation within the past view years. Their setups can be divided into two classes: one where the detection of Rydberg atoms is realised optically [18, 19, 20], involving an optical imaging system, and another where Rydberg atoms are ionised and imaged by an ion microscope onto a spatially resolving ion detector. In the latter category, Georg Raithel's group in Ann Arbor pioneered with a setup that uses the diverging electric field created by a high-voltage needle to ionise Rydberg atoms and obtain the necessary magnification [21]. A different method was realised by Jozsef Fortagh's group in Tübingen, that applies a sequence of electrostatic lenses [22] to magnify Rydberg ions onto the detector [23, 24].

A similar ion microscope is currently set up at the 5th Institute of Physics at the University of Stuttgart. It is part of an apparatus that will enable the generation of trapped, dilute ultracold clouds of rubidium and lithium atoms out of which Rydberg atoms will be photo-excited. After the actual Rydberg physics has taken place, the Rydberg atoms get ionised either with an electric field or via a V-shaped two-photon transition into the continuum [25]. The ion microscope together with the spatially- and temporally-resolving delay-line detector will eventually allow the observation of Rydberg physics in 3-D spatial resolution.

In order to calibrate the numerous electrodes along the microscope column and to test the microscope's resolution, a well-defined test pattern of ions is necessary. This can be generated by photo-ionising ground state atoms out of the ultracold cloud via a two-photon transition (see figure 1.1 for the case of  $^{87}\text{Rb}$ ) where e.g. the upper laser has a spatially-patterned intensity distribution such as that of an optical accordion lattice.

Within this thesis, a compact experimental setup for such an optical accordion lattice was designed, realised and characterised.

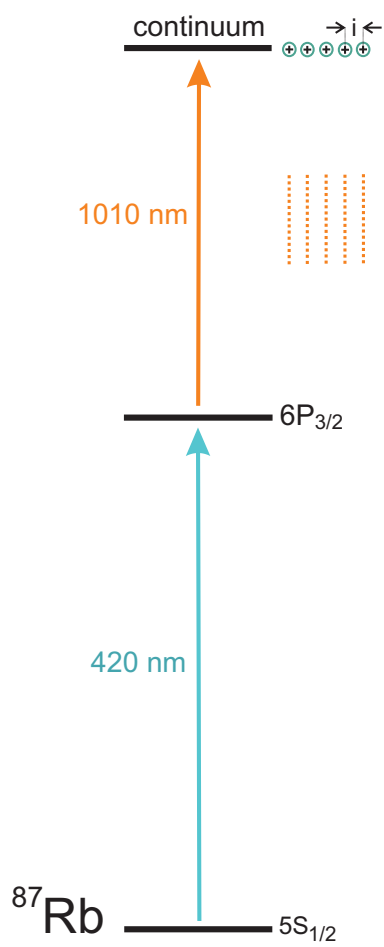


**Figure 1.1.:** Level scheme for the photo-ionisation of rubidium atoms to generate a tunable test pattern of ions with an optical accordion lattice (orange stripes, lattice periode  $i$ ). The resulting test structure can be used to calibrate and test an ion microscope.

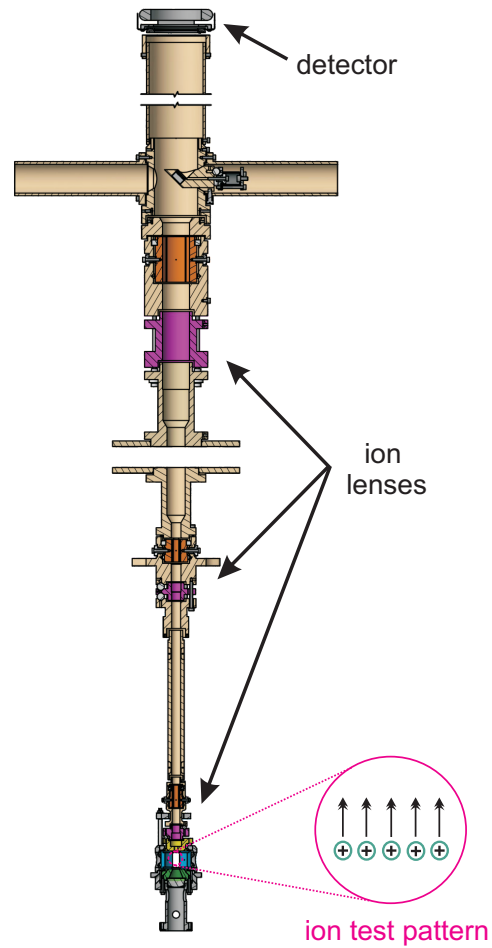


**Figure 1.2.:** Sectional drawing of the ion microscope to be calibrated and tested. The tunable ion test pattern will be prepared at the position where later the ultracold atomic cloud will be situated.

## 2. Theory

This thesis reports on a setup for the generation of an optical accordion lattice. To lay the theoretical foundations for the employed physical phenomena, this chapter will introduce basic information on laser light, geometrical optics and common components of optical setups. Furthermore, it includes a detailed description of the interference effect that leads to the creation of optical lattices. Eventually this chapter gives a short outline about the effect of thermal expansion which is important to describe the thermal stability of a system.

### 2.1. Laser

In 1917, Albert Einstein postulated the possibility of stimulated emission and thereby paved the way for the development of modern laser physics. Together with stimulated absorption and spontaneous emission, stimulated emission describes the basic processes that occur between two energy levels under the presence of external electromagnetic radiation. If an incoming photon of the external field couples to a transition between two levels with energy separation  $\Delta E = h\nu$ , where  $h$  is the Planck's constant and  $\nu$  the frequency of the incoming radiation, it can cause both an excitation into the upper level or a transition from the excited state into the ground state. In the latter case, the energy difference between the two levels is converted into a photon that has identical optical properties as the incident light, i.e. same frequency, phase, direction of travel and polarisation. This phenomenon can be technically utilized by building a device that emits spatially and temporally coherent light: a laser<sup>1</sup>.

#### 2.1.1. Working principle

Any laser consists of three main components that are displayed in figure 2.1. A pump supplies the system with energy that generates excitation and subsequent emission inside the active medium. While spontaneous decay happens on a larger timescale than stimulated emission, it gets mainly superseded by the latter. A resonator typically consists of one highly reflective and one partly transmissive mirror. It enhances amplification by back-reflecting the photons multiple times through the active medium before the laser light gets decoupled. It is crucial to successful laser operation that inside the active medium a population inversion is created i.e. that more electrons are in the excited than in the ground state. This cannot be achieved in a two-level system as the

---

<sup>1</sup>Light amplification by stimulated emission of radiation

external field drives transitions in both directions at the same rate. A three-level or even better a four-level system as shown in figure 2.2 makes a population inversion possible. The electrons get excited into a short-lived level from which they decay into the upper laser level. The latter needs to be long-lived to ensure the population inversion. After falling down into another short-lived level under emission of stimulated laser light, the electrons populate the ground state again and are ready for a new excitation cycle.

There are various laser designs involving different active media such as gases, liquids or solids and diverse resonator shapes and pump sources. In this thesis, a diode laser is used as a light source which is why the following section provides a more detailed description of this laser type.

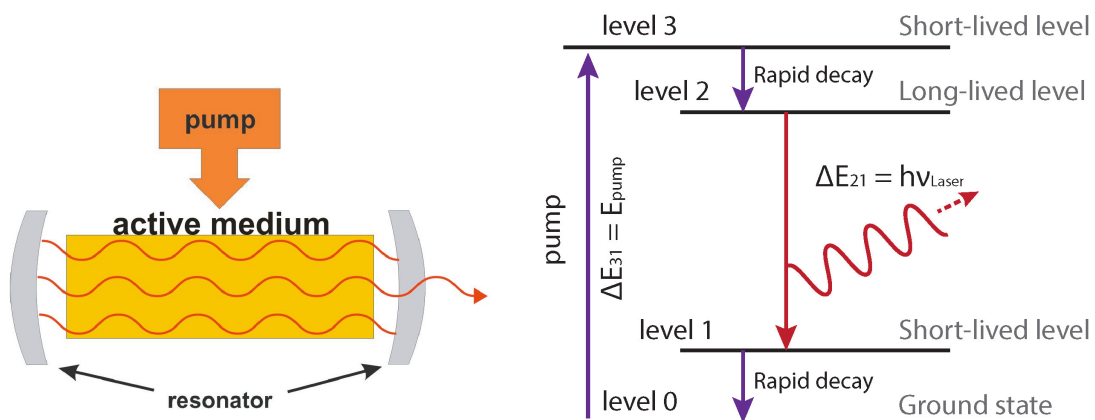


**Figure 2.1.:** Basic laser components. The pump delivers energy to create a population inversion inside the active medium. Most of the stimulated laser light is reflected between the resonator mirrors and contributes to amplification. A small part of it leaves the resonator via the partly transmissive mirror.

**Figure 2.2.:** Energy scheme of a four-level system with ground state, short-lived pump level, long-lived upper laser level and short-lived lower laser level. A population inversion is created between level 0 and level 2 in order to achieve laser operation. Figure taken from [26]

### 2.1.2. Diode laser

Diode lasers are based on semiconductor materials. In comparison to gas or solid-state lasers, their energy levels are broadened and can be described by energy bands that result from an overlap of the atomic orbitals. A distinction is made between the valence band that is ideally fully filled with electrons and a conduction band in which electrons can be excited. The energetic distance of the two bands ranges between 0.5 and 2.5 eV in common diode laser materials. Another feature of semiconductor physics is the definition of two kinds of charge carriers, namely electrons and

holes (missing electrons). Figure 2.3 shows the energy-momentum relation of the two particles resulting from a nearly-free carrier approximation which incorporates the carrier's interaction by introducing an effective mass for electrons and holes. The electron energies for small wavenumbers  $k$  in the conduction and valence band are given by the two parabolic functions

$$E_c = E_g + \frac{\hbar^2 k^2}{2m_e} \quad \text{and} \quad E_v = \frac{\hbar^2 k^2}{2m_h}, \quad (2.1)$$

where  $E_c$  and  $E_v$  refer to the valence and conduction band, respectively,  $E_g$  is the energy value of the bandgap and  $m_e$  and  $m_h$  are the electron and hole masses.

From figure 2.3, we can see that transitions between the valence and conduction band are linked to an absorption (excitation) or emission (decay) of a photon with energy  $\Delta E = \hbar\omega$  ( $\hbar$ : reduced Planck constant,  $\omega$ : angular frequency of the photon). These two processes correspond to generation and recombination of an electron-hole pair. As a photon's momentum is very small compared to that of an electron, the momentum change during a transition can usually be neglected, i.e. transitions can be drawn as vertical lines at a certain wavenumber in figure 2.3.

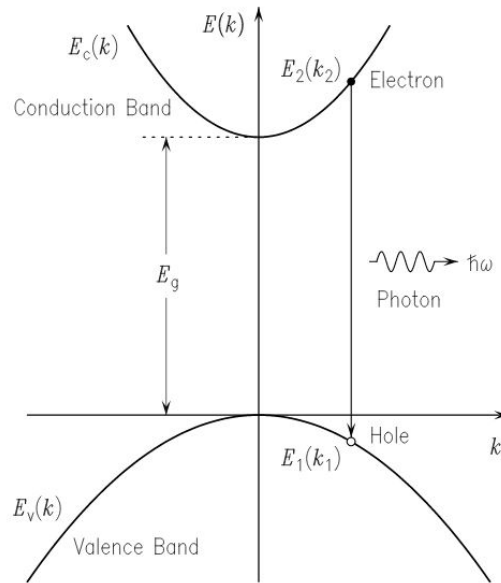


**Figure 2.3.:** Energy-momentum relation for electrons in the valence and conduction band of a semiconductor material. Excitation and decay from one band to the other is identified with an absorption and emission of a photon, respectively. Transitions occur at a single wavenumber as the photon's momentum is small compared to the electron's one and thus can be neglected. Figure taken from [27].

Although diode lasers can be pumped optically, the great advantage of this laser type is that pumping can be achieved by electrical current. There are again different designs of diode lasers that lead to stimulated laser emission. But generally speaking, the active medium consists of at least three semiconductor layers of which the outer ones are p- and n-type doped. Recombination happens inside the undoped middle layer which is therefore called the 'active zone'. Reflection of the emitted light is realised by either polishing or coating the sides of the semiconductor element or setting up an external resonator with mirrors. More elaborate semiconductor structures involve lateral confinement of the charge carriers.

A diode laser works like a normal forward-biased diode for small currents. Until a threshold current density  $j_{th}$ , spontaneous emission occurs. If this threshold current density is exceeded, laser activity gets started.

The laser wavelength depends on the band structure of the selected materials. This possibility of 'band gap engineering' is one of the great advantages of diode lasers and enables to build diode lasers for almost any wavelength within the visible spectrum and partly beyond. Efficiency often lies above 50 % which means that more than half of the electrical input power is converted into optical output power. One of the main detrimental factors is energy dissipation in form of ohmic heat.

A general property of all laser systems is the so called 'coherence length'. It describes the maximal path difference or difference in propagation time that two beams of the same light source can have to produce a spatially and temporally stable interference pattern. If the coherence length is exceeded, the interference pattern starts moving or vanishes.

## 2.2. Geometrical optics

When it comes to the description of light and its propagation through optical elements such as lenses, it is often expedient to use the picture of rays instead of waves. This approximation is only possible if the optical wavelength is small compared to the observed objects. As ray optics neglects the wave nature of light, it ignores effects like interference and diffraction. As will be shown in the subsequent section, many optical elements and their effects can be mathematically described by a matrix formalism in the framework of geometrical optics.

### 2.2.1. ABCD-matrix formalism

Matrix optics assumes that a propagating ray with no physical extent can be fully described by a distance  $r$  from the optical axis  $z$  and the slope  $dr/dz = \tan(\alpha)$ , where  $\alpha$  is the ray's angle with

the optical axis. Under the premise that  $\alpha$  is small at any position and time, one can make the so called ‘paraxial approximation’

$$\tan(\alpha) \approx \alpha$$

and the whole ray can be expressed by a two-dimensional vector  $\vec{a}$  with  $r$  and  $\alpha$  as its components. In this picture, optical elements like lenses are represented by 2x2-matrices that are multiplied with  $\vec{a}$  to give an outgoing ray vector  $\vec{b}$  with new properties. For a thin lens, i.e. a lens which has a small physical width compared to its radii of curvature, the mathematical description is given by the matrix

$$A_{\text{thL}} = \begin{pmatrix} A & B \\ C & D \end{pmatrix} = \begin{pmatrix} 1 & 0 \\ -\frac{1}{f} & 1 \end{pmatrix}, \quad (2.2)$$

where  $f$  is the focal length. Another useful matrix is the one of a translation of a distance  $d$ , i.e. free propagation of the beam between two optical elements:

$$A_{\text{trans}} = \begin{pmatrix} 1 & d \\ 0 & 1 \end{pmatrix}. \quad (2.3)$$

With these two matrices, one is already able to describe simple lens systems.

### 2.2.2. Lens systems

Sequences of lenses can be designed for a variety of applications. The focus of this section will be the magnification of

- the diameter of a collimated beam,
- an object.

The first case can be realised by a telescope configuration where two lenses are positioned in the distance of the sum over their focal lengths  $f_1$  as shown in figure 2.4. With the basic matrix concept of the previous section, the mathematical formulation is given by

$$\begin{pmatrix} r_2 \\ \alpha_2 \end{pmatrix} = \begin{pmatrix} 1 & 0 \\ -\frac{1}{f_2} & 1 \end{pmatrix} \begin{pmatrix} 1 & f_1 + f_2 \\ 0 & 1 \end{pmatrix} \begin{pmatrix} 1 & 0 \\ -\frac{1}{f_1} & 1 \end{pmatrix} \begin{pmatrix} r_1 \\ \alpha_1 = 0 \end{pmatrix} = \begin{pmatrix} -\frac{f_2}{f_1} r_1 \\ 0 \end{pmatrix}.$$

Hence, the outgoing beam is again collimated with  $\alpha_2 = 0$  and the magnification is described by the factor

$$M = \frac{f_2}{f_1}. \quad (2.4)$$

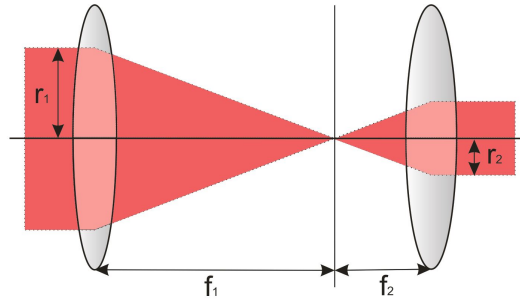


**Figure 2.4.:** Beam path inside a telescope consisting of two lenses with focal length  $f_1$  and  $f_2$  in a distance of  $f_1 + f_2$ .

The second case concerns the imaging of objects. If an object is very small and one wants to image it with a certain magnification  $\beta$ , one can use a lens system as shown in figure 2.5. Object distance  $g$  and image distance  $b$  need to match the lenses' focal lengths.

Again, matrices can be used to describe the system as follows:

$$\begin{aligned} \begin{pmatrix} r_2 \\ \alpha_2 \end{pmatrix} &= \begin{pmatrix} 1 & f_2 \\ 0 & 1 \end{pmatrix} \begin{pmatrix} 1 & 0 \\ -\frac{1}{f_2} & 1 \end{pmatrix} \begin{pmatrix} 1 & d \\ 0 & 1 \end{pmatrix} \begin{pmatrix} 1 & 0 \\ -\frac{1}{f_1} & 1 \end{pmatrix} \begin{pmatrix} 1 & f_1 \\ 0 & 1 \end{pmatrix} \begin{pmatrix} r_1 \\ \alpha_1 \end{pmatrix} \\ &= \begin{pmatrix} -\frac{f_2}{f_1} r_1 \\ \frac{d r_1 - (f_1 + f_2) r_1 - f_1^2 \alpha_1}{f_1 f_2} \end{pmatrix}. \end{aligned}$$

The resulting distance  $r_2 = -(f_2/f_1)r_1$  does not depend on  $d$ , which is why  $d$  is arbitrary, but it is scaled by a factor which gives the magnification

$$\beta = \frac{b}{g} = \frac{f_2}{f_1}. \quad (2.5)$$

For an enlargement, the condition  $f_2 > f_1$  has to hold.

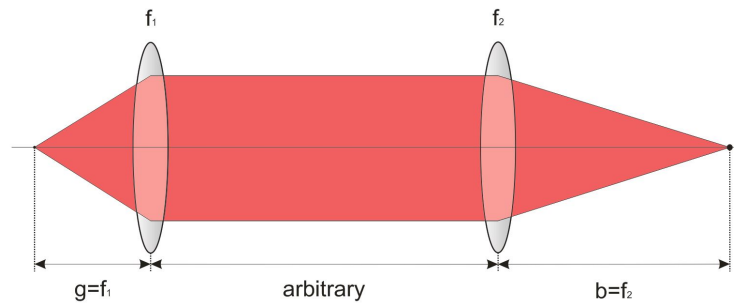


**Figure 2.5.:** Setup for imaging an object with a larger scale than the real proportions. Object distance  $g$  needs to be greater than image distance  $b$  while the distance of the two lenses is arbitrary.

### 2.2.3. Spherical aberrations

Aberrations are image defects that can arise from different error sources. One kind of aberrations holds for lenses with spherical surfaces and is called 'spherical aberration'. It implies that rays of different distances from the optical axis (i.e. centre and off-centre beams) have their focal plane at different points on the optical axis behind the lens (see fig. 2.6).

Aspheric lenses have at least one side which differs from a plane or spheric shape. Its surface is designed to compensate the spherical aberration effects. This makes aspheric lenses particularly interesting for optical applications with off-centred beams (see chapter 3.1).

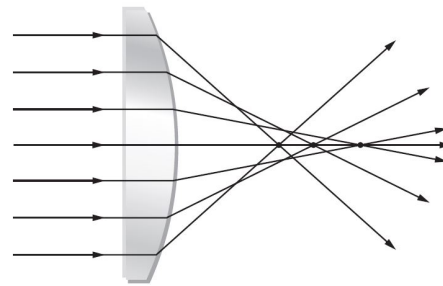


**Figure 2.6.:** Spherical aberration due to different focal planes of centre and off-centre rays.[28]

### 2.3. Polarising optical elements

Polarisation is a property of light as an electromagnetic wave which describes the orientation of the E-field<sup>2</sup> vector. For a transverse electromagnetic wave, it is useful to differentiate between the following states of polarisation:

- unpolarised light has E-field components in all the planes containing the propagation axis.
- linearly polarised light is oscillating in one specific plane containing the propagation axis.
- circularly polarised light has an E-field vector of constant magnitude which is rotating perpendicularly around the propagation axis.
- elliptically polarised light has an E-field that is rotating perpendicularly around the propagation axis but changes its magnitude at the same time. Looking in the propagation direction the vector's peak is moving on an elliptical orbit around the axis.

For any transverse electromagnetic wave which is propagating into the z-direction, the E-field vector stands perpendicularly on the z-direction and can be described by a superposition of two waves oscillating in x- and y-direction respectively. The cases of linearly, circularly and elliptically polarised light differ from each other by a phase delay  $\Delta\varphi$  between the two components  $E_x$  and  $E_y$ . Figure 2.7 gives an overview of the phase shift conditions for each polarisation state.

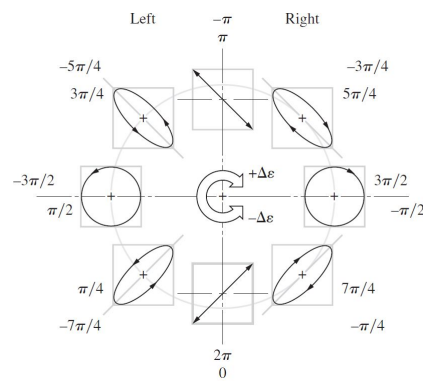


**Figure 2.7.:** Phase differences between x- and y-component of the electric field and the resulting polarisation over the range of  $2\pi$  [28].

If  $\Delta\varphi = n\pi$  for  $n$  being an integer, the light is linearly polarised. The magnitude of the single components determines the resulting orientation within the x-y-plane. For  $\Delta\varphi = (2n-1)\cdot(\pi/2)$  and equal magnitudes of the x- and y-components, the light becomes circularly polarised. All other combinations create elliptically polarised light. Waveplates consisting of birefringent crystals, such as calcite, can be used to manipulate the phase delay  $\Delta\varphi$  in order to change the polarisation. A so-called ‘half-wave plate’ can be used to rotate linear polarisation, whereas a quarter-wave plate turns a linearly polarised beam into a circularly polarised beam and vice versa [28].

<sup>2</sup>Electric field

A ‘polarising beam splitter cube’ is an optical element made of two triangular glass prisms with a coating in between the two hypotenuses. It splits an incoming beam into two single beams of which one gets reflected by  $90^\circ$  and the other gets transmitted. Usually, the transmitted beam comprises the E-field components parallel to the plane of incidence and is called the ‘p-polarised’ beam. The reflected beam is ‘s-polarised’ which means that its polarisation is perpendicular to the plane of incidence. Hence, a PBS<sup>3</sup> splits the light into two well-defined linearly polarised beams.

## 2.4. Gaussian optics

In the previous chapters light was either considered to be an electromagnetic wave or a set of straight rays without extent. The latter is a simplification that was improved by the concept of Gaussian optics where a ray is described as a so called ‘Gaussian beam’. The shape of a Gaussian beam is shown in figure 2.8 and 2.9. It is entirely defined by its smallest diameter which is called waist  $w_0$  at position  $z_0$  from which it broadens along the propagation axis  $z$ . For  $|z| \gg z_0$  the beam radius  $w(z)$  converges to a straight line that intersects the  $z$ -axis under an angle  $\theta/2$ .

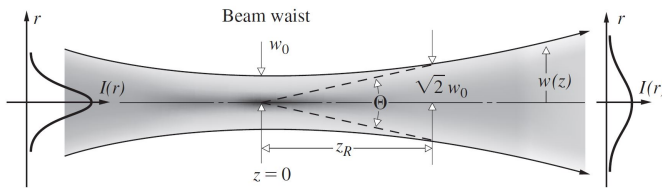


**Figure 2.8.:** Development of the Gaussian beam radius  $w(z)$  in front and behind the smallest value  $w_0$ . The Rayleigh length  $z_R$  is given by the distance from the waist position where the beam radius has a value of  $\sqrt{2}w_0$  [28].

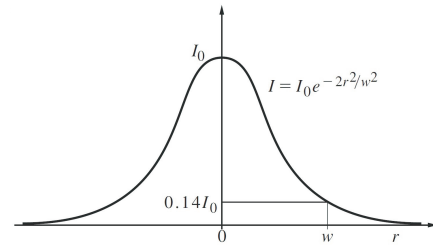


**Figure 2.9.:** Intensity distribution along  $r$  at a fixed position  $z$ . The width of a Gaussian beam can be defined by the position  $r$  where the intensity has dropped to  $I_0/e^2$ .  $I_0$  defines the maximal intensity in the beam centre [28].

The Rayleigh length describes the distance  $z_R$  from the waist position at which the waist has grown to a size of  $\sqrt{2}w_0$ . This is equivalent to the statement that the beam’s centre intensity has dropped to half of its initial value. Figure 2.9 shows the intensity distribution along the radial direction which is perpendicular to the propagation direction  $z$ . The transverse extend of the

<sup>3</sup>Polarising beam splitter

beam can be defined as the  $r$ -coordinate where the maximal value at  $r = 0$  has dropped to a value factorised by  $1/e^2$ .

The mathematical formulation of the Gaussian beam with polarization in x-direction is given by the electrical field

$$\vec{E}(r, z) = E_0 \hat{x} \frac{w_0}{w(z)} \cdot \exp\left(\frac{-r^2}{w(z)^2}\right) \cdot \exp\left(-i\left(kz + k\frac{r^2}{2R(z)} - \phi(z)\right)\right) \quad (2.6)$$

where  $r$  is the radial distance from the centre axis,  $E_0$  the amplitude at the origin and time  $t = 0$ ,  $k$  the wavenumber and  $\phi(z)$  the Gouy phase. The Gouy phase describes the phase shift that occurs when passing the focus.

The peak intensity of a Gaussian beam can be expressed by

$$I_{\max} = \frac{2 \cdot P_{\text{tot}}}{\pi \cdot w_0^2} \quad (2.7)$$

where  $P_{\text{tot}}$  is the total power which is transmitted by the beam [29].

For some applications it may be useful to describe the power of a Gaussian beam which is transmitted through a centred aperture with radius  $r$  transverse to the propagation direction of the beam at position  $z$ . The respective equation is given by

$$P(r, z) = P_{\text{tot}} \cdot \left(1 - \exp\left(-\frac{2r^2}{w^2(z)}\right)\right). \quad (2.8)$$

The ABCD-matrix formalism that was discussed above is also applicable to Gaussian optics. [30]. Instead of a ray vector, a complex beam parameter  $q$  for a Gaussian beam with propagation direction  $z$  is defined as

$$\frac{1}{q(z)} = \frac{1}{R(z)} - \frac{j\lambda}{\pi w(z)^2}, \quad (2.9)$$

where  $j$  is the imaginary unit and  $\lambda$  the wavelength that corresponds to the beam. The new beam parameter  $q_2$  can be expressed by

$$q_2 = \frac{Aq_1 + B}{Cq_1 + D}, \quad (2.10)$$

where  $A, B, C$  and  $D$  are the matrix components that were introduced for the ABCD-formalism. All matrices which describe optical elements remain unchanged (see subchapter 2.2.1) and can be used in this Gaussian extension of the formalism [29].

## 2.5. Accordion lattice

An optical lattice is an interference pattern created by two intersecting light beams. It can be associated with a standing wave of wavelength  $i$  as will be shown in section 2.5.1. Due to its periodic structure an analogy with a lattice can be drawn by attributing the positions of high intensity to lattice points and the zero (or low) intensity positions to the clearances in between. As previously shown by Li et al. [31], it will be demonstrated that the spacing  $i$  of the lattice points (which is identical with the former wavelength  $i$ ) depends on the angle  $\theta$  under which the two beams intersect. If  $\theta$  does not have a constant value but can be varied, the optical lattice becomes an ‘accordion lattice’.

### 2.5.1. Interference of two wavefronts

To demonstrate the principle of an optical accordion lattice, one can start from the picture of two intersecting plane waves. The formulas for two plane wavefronts with different propagation directions  $\vec{k}_1$  and  $\vec{k}_2$  and the same polarisation are given by

$$\Psi_1 = E_1 \cdot \exp\left(-j(\vec{k}_1 \vec{r} + \omega t + \varphi_1)\right) \quad (2.11)$$

$$\Psi_2 = E_2 \cdot \exp\left(-j(\vec{k}_2 \vec{r} + \omega t + \varphi_2)\right) \quad (2.12)$$

where  $E_{1,2}$  are the E-field amplitudes,  $\omega$  the angular frequency of the waves and  $\varphi_{1,2}$  individual phases.  $\vec{r} = (x, y, z)^T$  is the position vector. Using the definitions in figure 2.10 the two direction vectors can be defined as follows:

$$\vec{k}_1 = |\vec{k}| \cdot \begin{pmatrix} 0 \\ \cos(\theta/2) \\ \sin(\theta/2) \end{pmatrix} \quad \vec{k}_2 = |\vec{k}| \cdot \begin{pmatrix} 0 \\ \cos(\theta/2) \\ -\sin(\theta/2) \end{pmatrix}.$$

To calculate the intensity distribution, i.e. the interference pattern, at the intersection point, we first plug in the above vectors into equation (2.11) and (2.12). The z-dependent intensity distribution is then given by

$$I(z) = |\Psi_1 + \Psi_2|^2 = (\Psi_1 + \Psi_2)(\Psi_1 + \Psi_2)^* \quad (2.13)$$

$$= E_1^2 + E_2^2 + 2E_1E_2 \cos \left( \varphi_1 - \varphi_2 + 2 \left| \vec{k} \right| \sin \left( \frac{\theta}{2} \right) z \right). \quad (2.14)$$

As long as the phase difference  $\Delta\varphi = \varphi_1 - \varphi_2$  stays constant over time, the interference pattern will be stable in time and space.

The light intensity varies only over the lateral coordinate  $z$ . It oscillates between  $I_{\min} = (E_1 - E_2)^2$  and  $I_{\max} = (E_1 + E_2)^2$ . For equal electric field amplitudes of the two single beams ( $E_1 = E_2 = E$ ), the intensity margins become  $I_{\min} = 0$  and  $I_{\max} = 4E^2$ .

### 2.5.2. Lattice period

To overlap two beams with an angle  $\theta$ , two parallel beams are sent off-centered through a lens with focal length  $f$ , where they cross each other in the focal plane (see Ref. [31]). For a distance  $D$  of the two beams in front of the lens, the lattice period, which is equivalent to the term ‘lattice spacing’, can be derived from eq. (2.14) to have the form

$$i = \frac{\lambda}{2 \sin(\theta/2)} \approx \lambda \frac{\sqrt{D^2/4 + f^2}}{D}. \quad (2.15)$$

The approximation assumes that the beams are symmetric with respect to the axis of the lens and that they intersect in the focal distance  $f$ , so that the angle can be written as  $\sin(\theta/2) = 0.5 \cdot (D/\sqrt{(D/2)^2 + f^2})$ . The wavelength of the used light source is represented by  $\lambda$ .

As the beam size is finite and may not be clipped by the beam splitter edges, an arbitrary offset  $d_0$  is defined which gives the minimal distance of the beams to the symmetry axis and  $d$  as the new parameter. Substituting  $D = 2 \cdot (d + d_0)$  in equation (2.16) results in

$$i = \frac{\lambda}{2} \cdot \sqrt{1 + \left( \frac{f}{d + d_0} \right)^2} \quad (2.16)$$

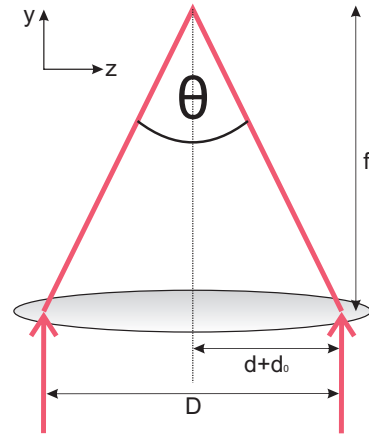


**Figure 2.10.:** Two laser beams intersecting under an angle  $\theta$  after passing a lens. The intersection point is defined to be at the position  $y = 0$ .

for the lattice period. With a setup which allows the variation of  $d$ , an optical lattice can be operated as an accordion lattice with tunable lattice period.

### 2.5.3. Visibility

One property of an optical lattice is its visibility  $C$ . It describes the quality of the discriminability between points of high and low intensity. Reference [29] gives its definition as

$$C = \frac{I_{\max} - I_{\min}}{I_{\max} + I_{\min}}. \quad (2.17)$$

If the contrast is perfect, i.e.  $I_{\min} = 0$ , the visibility has a value of 1. A value of  $C \rightarrow 0$  means that bright and dark spots have a similar value and are hence indistinguishable.

## 2.6. Thermal expansion

In general, most materials expand with increasing temperature  $T$ , although the extend of this phenomenon varies drastically.

One of the parameters that quantifies the effect of thermal expansion is the so called ‘linear expansion coefficient’  $\alpha_L$ . It is defined by

$$\alpha_L = \frac{1}{L} \frac{dL}{dT} \quad (2.18)$$

and describes how a body’s length  $L$  changes per degree of temperature change. Values for the linear thermal expansion coefficient of pure metals range between 4.5 and  $83.3 \cdot 10^{-6} \text{ K}^{-1}$  [32].

## 3. Experimental setup

The following chapter is dedicated to the experimental setup that was designed in the framework of this thesis. In section 3.1, the schematic setup is introduced, in the section 3.2 the experimental requirements are posed and section 3.3 is concerned with the realisation of the setup and its various features.

### 3.1. Schematic setup

As has been explained in chapter 2.5, to generate an optical accordion lattice it needs two beams with equal intensity and polarisation which cross each other under an arbitrary angle  $\theta$ . There are different possibilities to realise this in a setup. The schematic setup design used in this thesis was first introduced by the group of M. G. Raizen [31]. Figure 3.1 shows the whole beam path of the laser from the fibre outcoupler to the camera.

The beam, which leaves the fibre outcoupler, is collimated. For a sufficient size of the focal spot at the lattice position, the beam diameter needs to be downsized before it reaches an aspheric lens (Asphere ALL50-100-S-U, Asphericon GmbH) which creates the optical lattice in its focal plane. This is done right after the outcoupler with the help of two lenses in a telescope configuration that gives the magnification

$$M = \frac{f_2}{f_1} = \frac{50 \text{ mm}}{150 \text{ mm}} = \frac{1}{3}$$

(see equation 2.4). After the beam has passed the telescope, it gets reflected by  $90^\circ$  at a mirror which is mounted on a translation stage. The stage can be moved by a micrometer screw and will eventually change the distance of the two beams in front of the aspheric lens.

A PBS cube, which is also placed on the translation stage, ensures a linear polarisation of the beam. A second mirror reflects the beam onto two parallel PBS oriented as shown in figure 3.1. The ratio between reflected and transmitted beam inside a PBS depends on the incoming polarisation of the electromagnetic wave. In principle, it can be tuned by one half-wave plate. In the setup, two half-wave plates are used. One of them is placed directly in front of the PBS and is used for a coarse alignment of the polarisation. However, the mount of this half-wave plate does not allow a controlled fine-tuning of the rotation. This is the reason for another half-wave plate which is placed in front of the elliptical mirror. It ensures a nearly perpendicular polarisation of the light to the plane of incidence when it is reflected from the mirror, keeping the polarisation linear.

For proper adjustment of the half-wave plates, the first PBS cube reflects 50 % of the incident

beam and transmits another 50%. The transmitted p-polarised component passes the second cube without reflection. A two times transit through a quarter-wave plate turns the polarisation direction by  $90^\circ$  which leads to an entire reflection when the beam meets the second PBS cube again. The two beams are now running parallel and have a distance of  $2(d + d_0)$ . In this configuration, they reach the aspheric lens and get focused under the angle  $\theta$ . A 1:1 image of the lattice is obtained by placing the sensor of a camera directly in the focal plane of the lens.

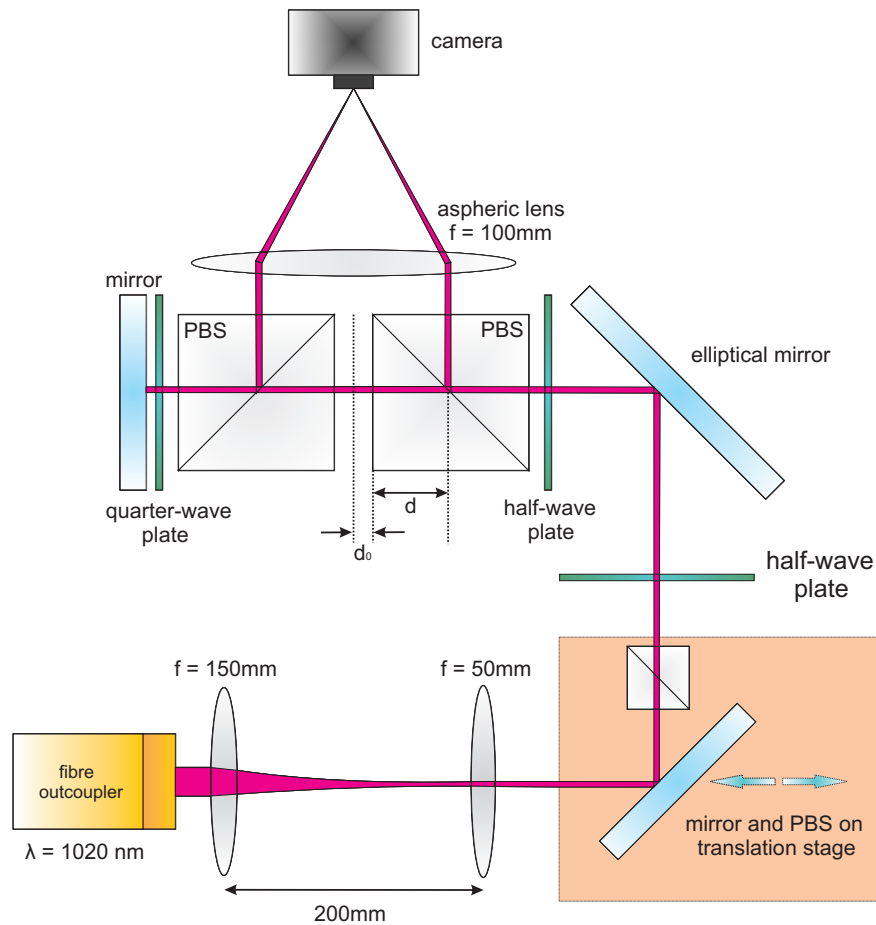


**Figure 3.1.:** Schematic setup to create an optical accordion lattice which is imaged by a camera in the focal plane of an aspheric lens. The beams in front of an aspheric lens are aligned parallel by two PBS and a quarter-wave plate. Equal intensities of the two beams can be obtained by the use of a half-wave plate before the incident laser beam reaches the cubes. Variation of the beam distance in front of the aspheric lens and thus a tuning of the lattice period is realised via a translation stage that shifts the beam's point of impact on the cubes.

## 3.2. Experimental requirements

The incorporation of the optical accordion setup into the architecture of the existing ion microscope experiment necessitates the fulfillment of several requirements.

To maximize the angle under which the two lattice beams can enter the vacuum chamber and at the same time keeping the lens dimensions within reasonable range, the whole setup needs to be placed as close as possible to the science chamber. While the aspheric lens with its focal length of  $f = 100$  mm needs to be mounted directly to the viewport of the science chamber (see adapter in appendix A), the remaining setup will be placed on an optics table in the direct vicinity of the chamber (see. figure 3.4). The constrained space on the optics table requires the setup design to be as compact as possible. Small dimensions and a modular design of the lattice setup have the side effect of simplifying its installation and operation. Optical access to the science chamber is limited to a small number of viewports which makes multiple usage of these windows unavoidable. This is also the case for the window through which the beams for the optical lattice will enter the chamber. Consequently, the setup design needs to leave space for additional laser beams to pass unfettered.

A further demand is a mechanically and thermally stable setup to ensure a reliable, well-defined interference pattern over several days.

## 3.3. Realisation of the titanium setup mount

To meet all requirements described in section 3.2, the entire central unit of the setup was arranged on a titanium mount. Figure 3.2 shows a 3-D model of the titanium box and labels the individual components.

In this configuration the overall dimensions could be reduced to a length, width and height of 126 mm, 70 mm and 62 mm, respectively, which is small enough to fit into the experiment environment.

In principle, the setup consists of only three mount parts and thereby features a straightforward almost monolithic design. To conserve the rotatability of the wave plates, the corresponding mounts needed to remain separate elements. The small and monolithic character of the setup is already a good foundation for thermal stability. Especially the critical distance for thermal expansion between the first PBS and the back-reflecting mirror was made as short as possible. A change in length on the order of the wavelength results in a relative phase shift of the two interfering beams, changing the fringe positions. However, the largest contribution for obtaining thermal stability is given by a well-considered choice of the mount material. Titanium is features

a comparably low linear thermal expansion coefficient of  $\alpha_L = 8.6 \cdot 10^{-6}/\text{K}$  [33]. This is by almost a factor three better than aluminum ( $\alpha_L = 23.1 \cdot 10^{-6}/\text{K}$ ). Other materials like invar ( $\alpha_L = 1.5 \cdot 10^{-6}/\text{K}$ ) outperform titanium in this regard, but they are usually either unhandy for mechanical processing or show strong magnetism. The latter is unsuitable for the use in the experiment, because the setup is close to strong magnetic fields produced by the Feshbach coils for lithium and would influence these magnetic fields.

As the sufficiency of passive thermal stability still had to be tested, the conceptual setup design provides foundation for further passive and active stability enhancement. For one thing, several screw holes were placed at each side of the setup to enable optional cladding of the central unit and shield it from both temperature changes and dust. For another thing, two symmetric holes for temperature sensors were planned at the sides along the critical section. In case of need for active temperature stabilisation, Peltier elements can be attached to the sides of the setup while the temperature is measured inside the mount material. The Peltier elements can be used to heat the titanium box to a constant temperature.

One of the experimental requirements regarded laser beams for other purposes like Rydberg excitation and trapping of the atomic cloud. These beams need to enter the science chamber through the same viewport as the beams that create the optical lattice. To enable their unaffected optical access to the chamber, a slot of 6 mm width was planned between the two beam splitter cubes. It makes it even possible to deploy a laser beam with an exaggerated vertical extent which could be used to create a light sheet to further confine the optical lattice to a two-dimensional structure.

The adjustment of the mounted optical elements does not allow for all degrees of freedom. In order to do all necessary alignment to overlap the lattice with the atomic cloud, a miniature 5-axis stage under the titanium box is used. This allows yaw, tilt and the shift of the entire unit in all three spatial directions.

As can be seen in figure 3.2, the elliptical mirror is mounted on a separate part which is screwed to the titanium mount. This leaves the option to replace it by a smaller movable mirror, which would substitute the translation stage in figure 3.1. Such an adaptation would enable further diminution of the setup as the extended platform on the right side in fig. 3.2 could be shortened. All the mount components were manufactured by the University's mechanical workshop. Pictures 3.3 a) and b) display the holders for the waveplates. To further reduce the critical distance between first PBS and back-reflecting mirror, the mirror was incorporated into the waveplate holder (see fig. 3.3 b). Picture c) shows the assembled setup.

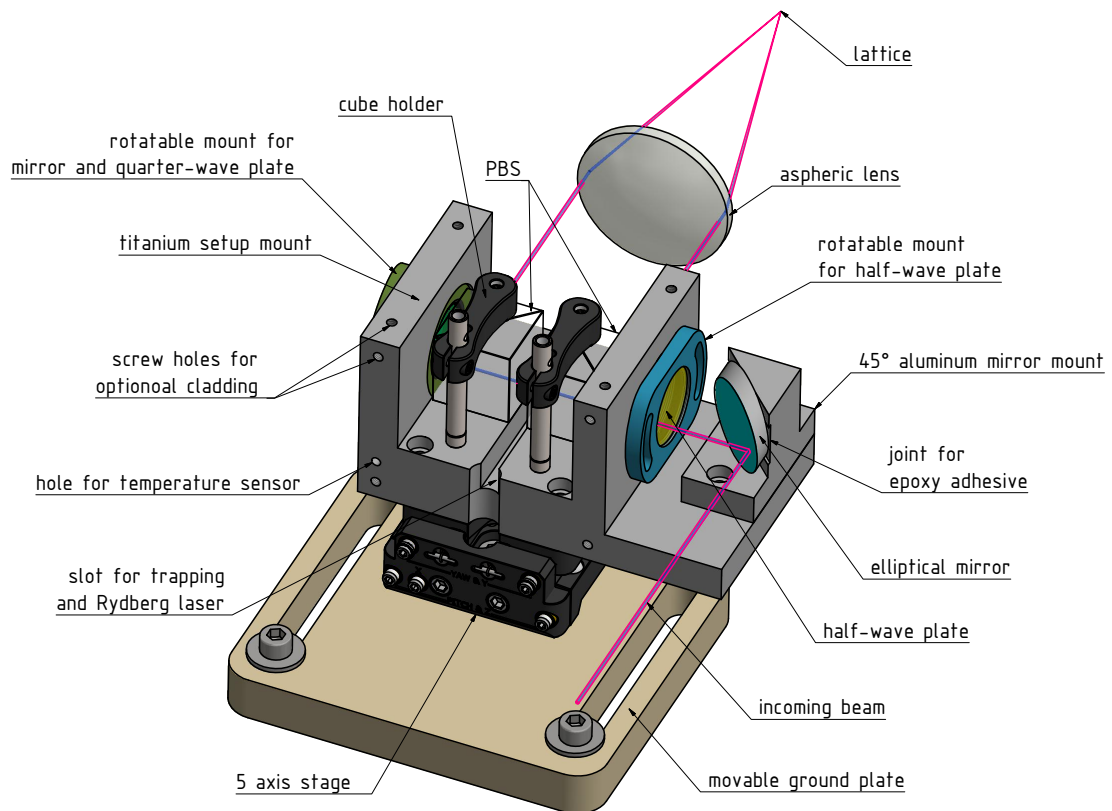
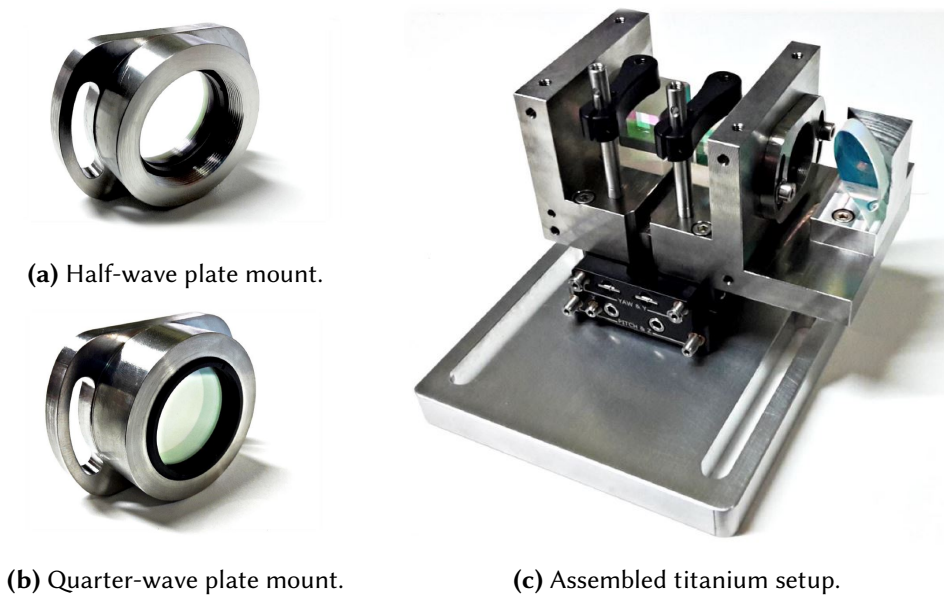


Figure 3.2.: Conceptual setup design.



(a) Half-wave plate mount.

(b) Quarter-wave plate mount.

(c) Assembled titanium setup.

Figure 3.3.: Pictures of the manufactured titanium components to mount the half-wave and quarter-wave plates and the assembled titanium setup mounted on the 5-axis-stage.

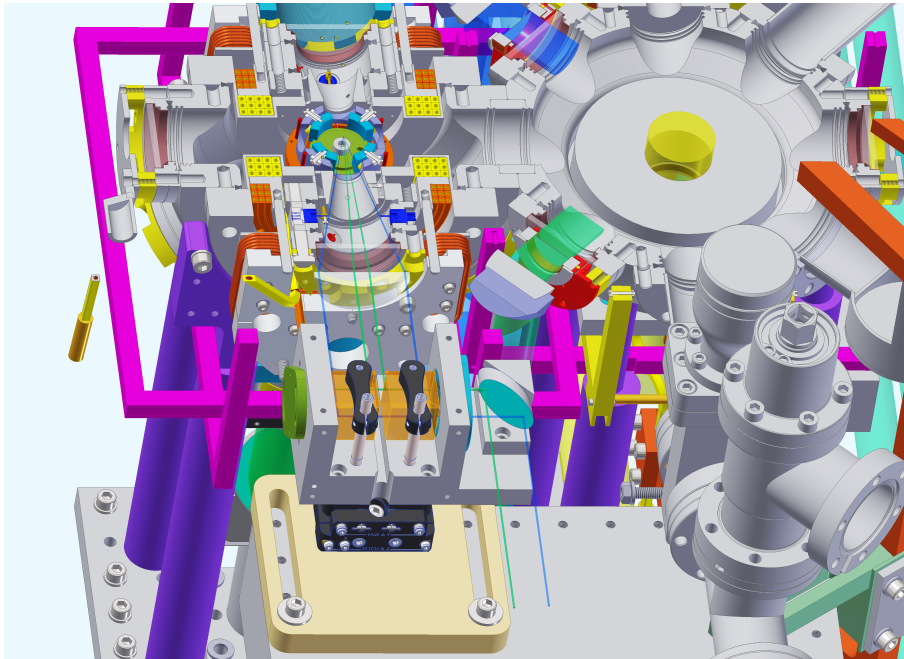


**Figure 3.4.:** Conceptual setup design integrated in the current environment of the ion microscope experiment. Behind the central setup unit one can see a sectional drawing of the science chamber.

## 4. Results

In the framework of this thesis, a setup to create an optical accordion lattice was designed and built. The following chapter comprises beam path simulations that were done to estimate the transverse extent of the created lattice (section 4.1). Furthermore, it reports on the characteristics of the Raspberry Pi camera used to image the optical lattice (section 4.2). Section 4.3 includes the characterisation of the obtained optical accordion lattice. It shows the achievable range of the lattice period, the transverse intensity profile and its visibility and the evolution of the pattern at positions in front and behind the intersection point of the two beams. Additionally, the thermal stability of the setup is addressed.

### 4.1. Simulations

Preliminary to the experimental measurements taken with the accordion lattice setup, the optical setup was simulated in order to find appropriate laser beam diameters and to estimate the effect of optical aberrations caused by the aspheric lens.

#### 4.1.1. Transverse diameter of the optical lattice

In order to find an appropriate diameter of the lattice beams, it was assumed that the atomic cloud in the centre of the science chamber has an approximate size of  $100 \mu\text{m}$ . It is then desirable to create an optical lattice with a transverse extent of roughly  $300 \mu\text{m}$  to ensure covering the whole cloud.

A Gaussian beam simulation programme (GaussianBeam) was used to model the lens system described in chapter 3.1 and to determine the waist of the laser beams behind the aspheric lens. To feed the programme with initial data, the beam diameter behind the fibre outcoupler had to be calculated. Therefore, the output power  $P_{\text{tot}}$  was measured directly behind the outcoupler. Another power measurement  $P_{\text{iris}}$  was conducted behind an iris with a diameter of  $r = 1 \text{ mm}$  which was placed symmetrically in the beam path behind the outcoupler. Rearrangement of equation (2.8) gives a formula for the waist of the beam. It is

$$w = \sqrt{-2r^2 \cdot \frac{1}{\ln\left(1 - \frac{P_{\text{iris}}}{P_{\text{tot}}}\right)}} \approx 0.58 \text{ mm}.$$

Thus, the beam diameter was determined to be  $d_{\text{beam}} \approx 1.16$  mm.

The simulated beam path through the two telescope lenses and the aspheric lens is displayed in figure 4.1. The waist position of the input beam was assumed to lie at the position of the fibre outcoupler which was defined as  $z = 0$ . All simulated lenses were positioned at distances which match with their real positions in the setup. The values for the waists behind each lens are given by  $w_i$ .

The most relevant value is the focal spot size  $d_3 = 257.4 \mu\text{m}$  of the beam behind the aspheric lens. This is close to the desired value. The waist position at a distance of  $\Delta z = 143.3$  mm from the lens is not identical with the focal length  $f = 100$  mm. This is due to the divergence of the beam before the aspheric lens.

The Rayleigh length of the beam behind the aspheric lens was determined to be  $L_R = 5.1$  cm.

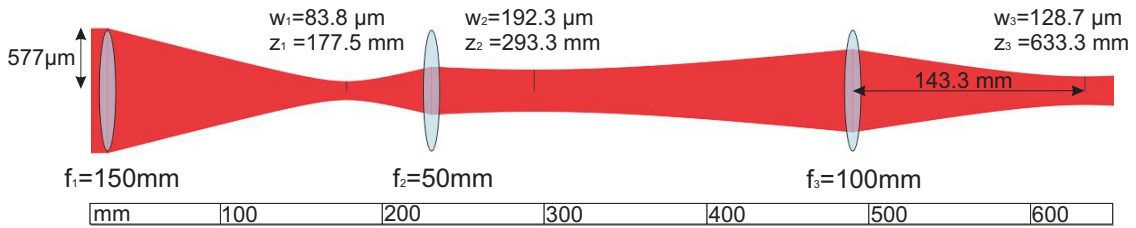


**Figure 4.1.:** Simulated beam path from fibre outcoupler to the focal position after the aspheric lens.

#### 4.1.2. Focal shift between centre and off-centre beams

To minimize spherical aberrations, an aspheric lens was employed to focus the two beams. Nevertheless, there is a non-vanishing focal shift between beams hitting the lens at different distances from the optical axis. In order to obtain an estimate for the aberrations that have to be expected for the selected lens model, a Zeemax simulation was conducted. Data for the aspheric lens was provided by the manufacturer (Aspericon) and the wavelength used for the simulation matches the  $1020 \text{ nm}$  wavelength of the laser used in the real setup.

In the simulation, the intersection of the rays with the optical axis was evaluated for rays hitting the lens at different radial distances from the optical axis with a maximum distance of  $23 \text{ mm}$ . The simulations showed that the predicted shift remains within  $\Delta z = 10 \mu\text{m}$ .

## 4.2. Characterisation of the Raspberry Pi camera

The Raspberry Pi Camera v2 (hereafter ‘Pi camera’) has been chosen to image the lattice in the focal plane of the aspheric lens. This choice is mainly reasoned in the small pixel size of  $1.2 \mu\text{m}$  that is necessary to obtain images of even the smallest lattice spacings resolved. However, the Pi camera is not a high-end scientific camera with linear input-output characteristics.

To determine the range in which the intensity values scale linearly with the laser intensity, a characterisation has been done that is displayed in figure 4.2. For this, only one of the two beams was directed onto the camera and its power was varied, so that a common beam profile was depicted on the camera’s sensor instead of a lattice.

As the camera has an 8-bit resolution, the brightness values range between 0 and 255. As a first step, the measured power data was converted into intensity values by equation (2.7). For this, the beam waist was determined by summing up the brightness values of a beam spot in one direction. This resulted in a Gaussian distribution and by fitting the data, a waist of  $w \approx 232.5 \mu\text{m}$  was gauged.

Up to approximately  $0.025 \text{ mW/mm}^2$ , one can see a steep increase of the brightness that flattens a bit for the following  $0.06 \text{ mW/mm}^2$ . From  $0.085 \text{ mW/mm}^2$  onwards, the brightness shortly stays on a constant level and then rises again until it saturates on the highest value of 255 at around  $0.18 \text{ mW/mm}^2$ . The blue dashed line indicates the highest brightness value that was found in the spot centre, whereas the red line shows a mean value of the 16 pixels surrounding and containing the pixel with the highest value.

Although nonlinearity is visible over the whole measurement range between 0 and  $0.378 \text{ mW/mm}^2$ , we can assume an almost linear region from  $0.025$  to  $0.085 \text{ mW/mm}^2$ . Before implementing this knowledge in future measurements one has to consider the following: Only one beam was used for the measurement. As the lattice is created by two beams, the intensity will be multiplied by two. Another factor of two arises from the interference term of equation (2.14) for maximal intensity which equals  $2E^2$  (provided that  $E_1 = E_2 = E$ ). Consequently, the chosen beam intensity needs to be divided by four in order to make sure not to leave the linear range at any position of the camera’s sensor chip. This means that the intensity has to be set on a value between  $0.007 \text{ mW/mm}^2$  and  $0.021 \text{ mW/mm}^2$ .

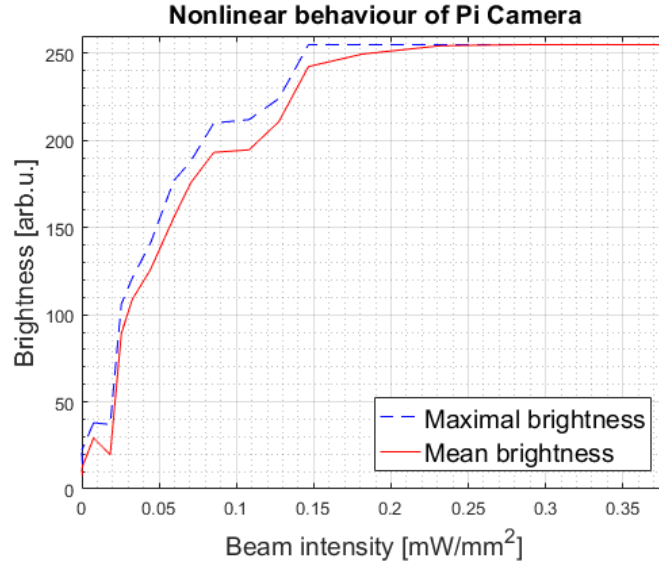


**Figure 4.2.:** Brightness values of the camera pixels for increasing laser intensities. The beam intensity was calculated from power data that was measured in front of the camera sensor. Maximum brightness is associated with the highest brightness values in the pictures and mean brightness refers to the mean values of 16 pixels surrounding the highest data point. For this characterisation, half of the beam was blocked after it was split up by the PBS.

### 4.3. Lattice characterisation

#### 4.3.1. Variation of lattice period

The aim of this subchapter is to validate the accordance of the measured data with formula (2.16) that predicts the change in lattice period at simultaneous translation of stage from figure 3.1. The experimental requirements entail certain limitations on the maximal spacing of bright bars. Large spacings are given for small angles between the two intersecting beams. As the setup leaves a slit of 6 mm size for other laser beams between the two BPS this value also identifies the smallest beam distance. Additionally, the beam diameter has a finite value of approx.  $400 \mu\text{m}$  when passing the cubes. In theory that adds another  $400 \mu\text{m}$  to the smallest beam distance for which the beams are not clipped when being reflected or transmitted. As the cube edges are not ideal but slightly radiused a larger value of 1 mm was estimated for the simulation plotted in figure 4.3. In the region of particular small spacings one boundary is given by the camera's resolution. The pixel size of  $1.12 \mu\text{m}$  theoretically allows an imaging of lattices with period  $2 \cdot 1.12 \mu\text{m} = 2.24 \mu\text{m}$  which is hard to achieve in real-life as maximum and minimum of the wave would have to match

perfectly with the center of their pixels in order to gain a sufficient visibility. Practically, that will most probably not be the case and instead one would see, if at all, a strongly blurred pattern.

Nevertheless, this problem counts only for the imaging of the lattice. Looking at the future experimental implementation the resolution argument gets obsolete as single atoms in a cloud range on way smaller length scales. In respect thereof, another limitation may be quoted that stems from the science chamber's geometry. The viewport window is framed by parts that enable only a maximum beam angle of  $\theta = 27.18^\circ$  if the asphere is placed at the correct working distance of 93.4 mm from the chamber's centre. Converted into a beam distance, the respective value is  $d_{\max} \approx 23$  mm. Figure 4.3 shows the theoretical lattice period (blue curve) for a 1020 nm light source where  $d_0$  is identified

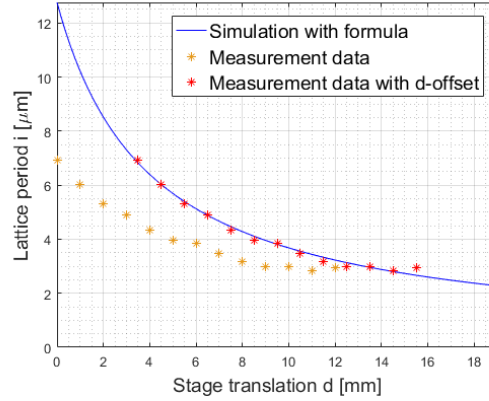


**Figure 4.3.:** Anticipated (blue curve) and measured (asterisked) lattice periods at varying stage positions  $d$ . The measurement was limited by the PBS edges for large spacing and the camera resolution in the region of small spacing.

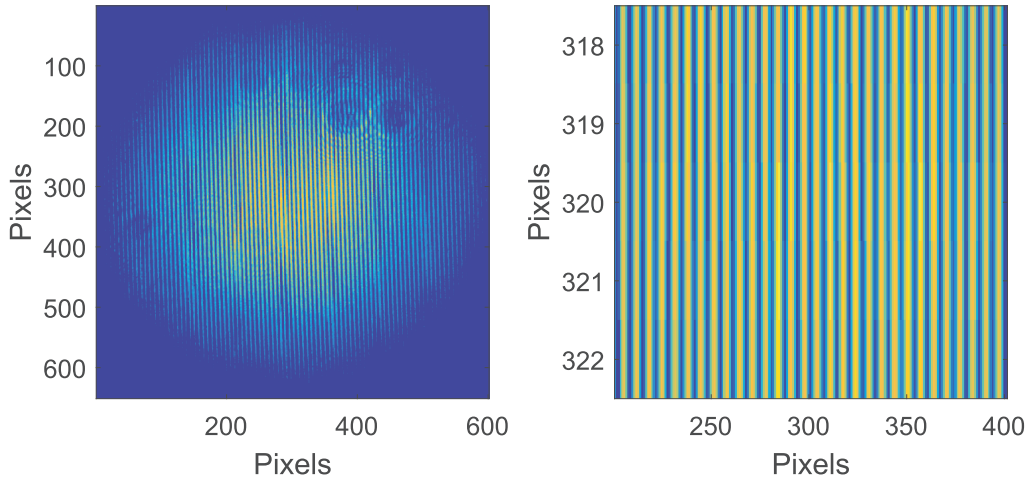
with 4 mm and the stage translation range equals 19 mm.  $d = 0$  refers to the stage position with maximal lattice period. Besides, the measurement data is plotted with orange asterisks and comprise the stage translations where the two laser beams have a Gaussian profile (i.e. are not clipped) and a lattice pattern is discernible. The displacement of the measured behaviour towards small  $d$  indicates that the real minimal beam distance from the centre between the cubes is larger than 4 mm, namely 7.5 mm. This is due to the radiused corners of the cubes and suggests the assumption that the beam diameter is already a bit larger at that point than anticipated.

Adjusting the data to the theoretical regime of the blue curve by adding a  $d$ -offset of 3.5 mm (red asterisks) illustrates that the experimental data fits to the analytical simulation except for the last point at smallest spacing. Here, the camera's resolution limit is already noticeable. A lattice spacing of  $3 \mu\text{m}$  means that 2.68 pixel need to display a whole lattice period.

In summary it can be said, that the achieved period range is smaller than what the theory predicts. This is due to both setup boundaries and imaging limitations. While the former is also valid when using the accordion lattice setup for calibration purposes in the ion microscope experiment, the latter only confines the possibility to give evidence about the lattice's quality and structure. However, the range between 7 and  $3 \mu\text{m}$  lattice period is sufficient for first conservative assessments of the ion microscope's resolution and should enable thorough calibration.

### 4.3.2. Field of view

In this chapter, the optical lattice will be analysed in terms of brightness distribution in both horizontal and vertical direction and the visibility will be calculated for the entire field of view. As the images give most detailed information for large lattice periods, the characterisation was done for a lattice spacing of approximately  $6.5 \mu\text{m}$ .



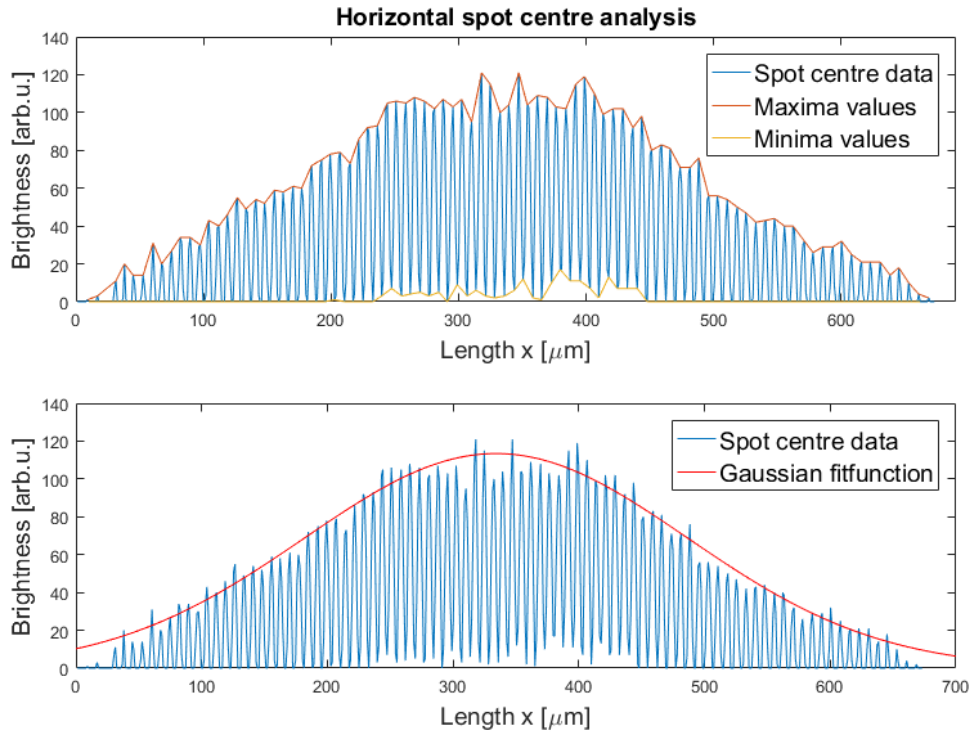
**Figure 4.4.:** Image of the lattice spot that was taken by the Raspberry Pi Camera (left) and extracted horizontal line of the spot centre (right).

Figure 4.4 (left) displays an image of the lattice spot that was taken by the Pi camera in the focal plane of the aspheric lens. The color code ranges from dark blue to yellow, where yellow indicates high laser intensity and blue low intensity. The circular interference patterns which occur at the upper right and left area of the picture stem from the camera chip. Most probably they can be attributed to dust particles that have settled down on the chip's surface.

The left image of the figure shows the brightness along 5 pixel rows that were taken out of the spot centre. A distinct lattice structure is visible as well as a clear increase of brightness towards the centre. Theory suggests, that the brightness profile of the lattice spot has again a Gaussian shape ([31]). This assumption is confirmed by the fit functions which approximate the horizontal spot profile in figure 4.5 (bottom) and the vertical profile in figure 4.6. Both fits were conducted with the Gaussian fitfunction

$$f(x) = a \cdot \exp\left(-\left(\frac{x-b}{c}\right)^2\right). \quad (4.1)$$

The peak value is represented by parameter  $a$ ,  $b$  refers to the horizontal offset of the function and  $c$  can be associated with the waist of the spot. The latter is of particular interest as it gives the physical extent of the lattice. In contrary, the peak value  $a$  does not give an absolute value as it is dependent on the camera's exposure time, ISO-settings, etc. These parameters are not calibrated. One could determine a reliable peak value by measuring the beam power and assuming a Gaussian distribution as it has been done for the Pi camera characterisation.



**Figure 4.5.:** Analysis of the spot centre line in figure 4.4 (right). The upper plot shows the brightness data as well as maxima and minima values as a guide to the eye. In the bottom plot the maxima values were fitted by a Gaussian function (see. eq.(4.1)) to give an envelope for the brightness data.

The Gaussian fit in figure 4.5 was calculated for the maxima values that are displayed as the orange curve in the upper plot. Its function is given by

$$f_h = (113.4 \pm 2.5) \cdot \exp\left(-\left(\frac{x - (334.2 \pm 3.9)}{(215.4 \pm 5.8)}\right)^2\right). \quad (4.2)$$

This means, that the horizontal extend of the lattice equals  $\Delta x = (215.4 \pm 5.8) \mu\text{m}$ .

The data in figure 4.6 was created by summing up the brightness values of figure 4.4 (left) in horizontal direction. This gives the brightness distribution in vertical direction. Analogously to the horizontal distribution, the data was fitted to give the function

$$f_v = (1.814 \pm 0.009) \cdot 10^{-4} \cdot \exp\left(-\left(\frac{x - (364.2 \pm 0.7)}{(180.9 \pm 1.0)}\right)^2\right), \quad (4.3)$$

which gives a vertical spot extend of  $\Delta_y = (180.9 \pm 1.0) \mu\text{m}$ . However, the values for  $\Delta_x$  and  $\Delta_y$  have to be treated with caution due to the camera's non-linear input-output behaviour that was discussed in chapter 4.2.

The visibility of the lattice can be understood as the quality of the contrast between the peaks of high and low intensity. It was calculated along the horizontal line of figure 4.4 (right) by using equation (2.17) and is displayed in figure 4.7. The values for maxima and minima are displayed in the upper plot of figure 4.5 as red and yellow lines, respectively. Every visibility data point was calculated for a neighbouring pair of maximal and minimal brightness.

One can see that the visibility has an ideal value of  $C = 1$  in the outer regions of the lattice. In the centre part it drops for several data points to values between  $C = 0.75$  and  $C = 0.98$ . Hence, in total the visibility always remains on a level above 75 %. To achieve a

visibility of one, the minimum intensity of the interference pattern needs to vanish. This is the case for an ideal optical lattice which created by two beams with both equal intensity and polarisation. In the setup at hand, the beam intensities were controlled by two half-wave plate. Nevertheless, as the adjustment precision was limited to alignment by hand, a totally equal beam intensity can not be provided. As a detrimental factor to this case, the intensity equality was determined by measuring the power of the two single beams behind the aspheric lens. The power meter could only be used to analyse one beam at a time. Hence, the waveplate could not be adjusted while looking at the two power values simultaneously. In order to minimize the resulting error, a second

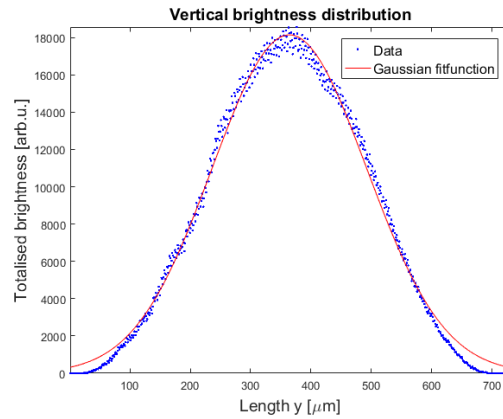


**Figure 4.6.:** Analysis of the vertical beam spot profile. The brightness values of the spot image in fig. 4.4 (left) were totalised in horizontal direction and plotted over the vertical length. The displayed fitfunction has a Gaussian shape according to eq.(4.1).

half-wave plate in a rotation mount was placed between the first PBS and the elliptical mirror. It serves to conduct fine-tuning of the polarisation ratio after the second waveplate was adjusted close to the optimum. The first waveplate's rotation mount gives the possibility to adjust the waveplate more precise than the titanium mount does. This method led to an improvement of the visibility and was already done for the displayed data in figure 4.7.

Polarisation equality of the two beams is ensured by the two PBS in front of the aspheric lens. However, only the p-polarised component has a very well-defined polarisation, whereas the s-polarised component is slightly impure. Theoretically, this problem can be solved by placing an additional PBS behind each of the two main cubes. This approach was tested but did not show any observable effect.

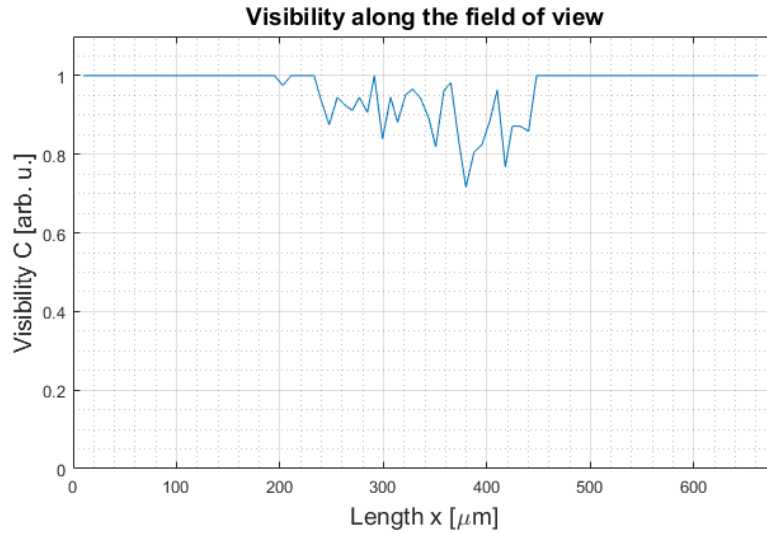


**Figure 4.7.:** Visibility along the central line of the spot in fig 4.4. It was calculated by using equation (2.17) and taking neighbouring maxima and minima.

### 4.3.3. Depth of field

In the experimental setup, the atomic cloud has to be aligned with respect to the axis of the ion microscope, the centre of the electric field control and the accordion lattice. In this section, the depth of field is analysed to determine the degree to which the intersection point of the two laser beams has to be aligned with the atomic cloud.

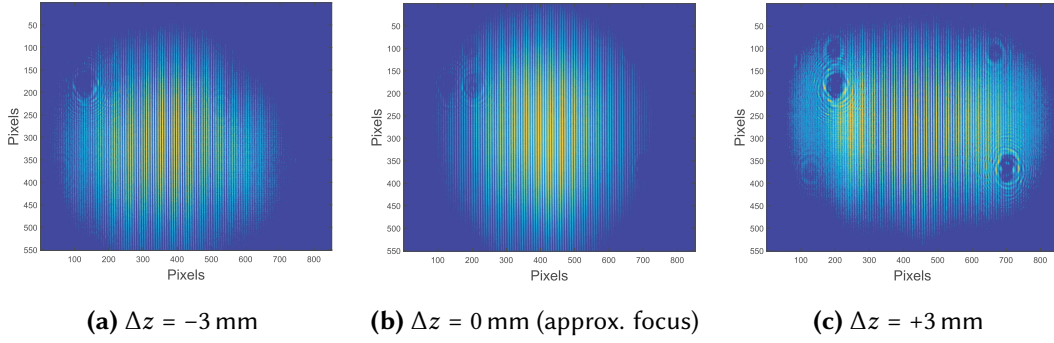


**Figure 4.8.:** Lattice images for different positions of the camera along z-direction. Image a) displays an offset of  $\Delta z = -3$  mm, b) shows the approximate position where the two beams intersect and c) is the image for  $\Delta z = +3$  mm.

To measure the range, in which one can still observe a lattice pattern of high visibility, the camera was moved towards ( $\Delta z > 0$ ) and away from ( $\Delta z < 0$ ) the aspheric lens around the position where the two beams intersect. Figure 4.8 shows three camera images that were taken at the limits of the analysed range  $[-3$  mm,  $+3$  mm]. The margins were chosen as a conservative estimation of the precision that can be achieved for the position of the atomic cloud.

The  $z = 0$  position was defined by placing the camera in the position with the smallest spot size. The Rayleigh length of the laser beams after the aspheric lens is 5.1 cm as shown by the beam path simulation in chapter 4.1.1. This leads to uncertainties of the  $z = 0$  position of  $\pm 0.75$  mm which explains the asymmetry of the two pictures 4.8 a) and c) that were taken behind and in front of the estimated crossing point, respectively.

Furthermore, it needs to be stated that the information given in this chapter holds only true for the used lattice period of  $7 \mu\text{m}$ . In the case of smaller lattice periods, the two laser beams intersect under a larger angle and the overlap of the two diminishes already at shorter distances. Already by having a look at the displayed pictures in figure 4.8 one can tell, that the lattice pattern remains distinct in the spot centre where the two beams have still a sufficient overlap.

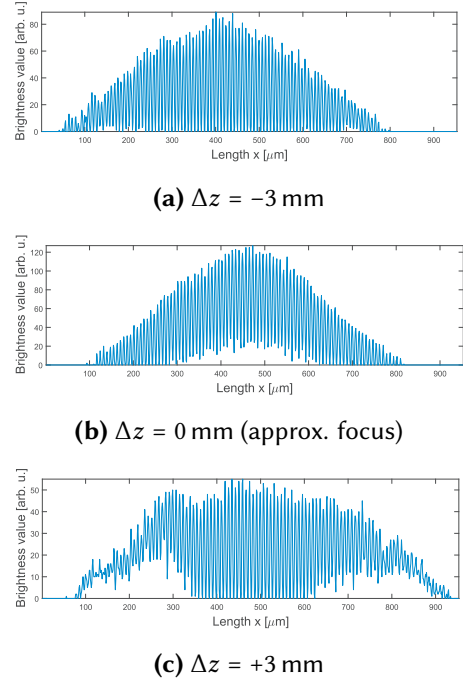


**Figure 4.9.:** Lattice profiles for three different positions of the camera along z-direction.

Horizontal profiles through the spot centres are plotted in figure 4.9 a) to c). The extract from the approximate focal position in 4.9 b) has a similar shape as the analysed lattice in figure 4.5. The rise of minimal intensities towards the spot centre are caused by an imperfect adjustment of the single beam intensities. In the outer regions of the beams, the insensitivity of the camera hides the imperfect destructive interference.

In figure 4.9 a) and c) the lattice pattern becomes more and more faint as the overlap of the two beams vanishes. In plot c) this phenomenon is more pronounced which indicates that the real focal position lies between  $\Delta z = -3$  mm  $\Delta z = 0$  mm.

It can be concluded that within a small range of  $\pm 3$  mm in front and behind the crossing point of the two beams the optical lattice is still well-defined enough to create a distinct ionisation pattern.

#### 4.3.4. Thermal stability

As it counts for any experiment involving interferometry of optical wavelengths, one main challenge of this Bachelor thesis was the thermal stability of the setup. Considering the sections of the optical path where the two beams take different ways, it becomes apparent that the critical region contains the second PBS, the quarter waveplate and the mirror. It is crucial to the stability of the lattice position that the phase difference  $\Delta\varphi$  between the two paths remains constant which is the case as long as the beam paths do not change unequally over time.

Apart from mechanically induced vibrations the main cause of shifts in the phase relation is temperature change. As will be shown in the following subchapters, the temperature inside the laboratory varies by about 1.6 K within 24 hours.

There is no easy way to influence the temperature dependency of the optical elements other than thermally isolating them, but they anyway do not react very sensitive to temperature changes in moderate temperature regimes. However, there are two ways to counteract the thermal expansion of the mount material:

- Active stabilisation by tracking the phase shift and readjusting the optical path length. Adjustment can be realised by using for example a piezo crystal that is actuated by a PID<sup>1</sup> controller [34].
- Passive stabilisation by choosing a material which is insensitive to temperature fluctuation i.e. has a low linear thermal expansion coefficient  $\alpha_L$ .

In this thesis the latter approach was taken. There are various materials with very low thermal expansion coefficients such as Zerodur ( $\alpha_L < 0.1 \cdot 10^{-6}/K$  [35]) or Invar ( $\alpha_L = 1.18 \cdot 10^{-6}/K$  [32]).

---

<sup>1</sup>Proportional-integral-derivative

The former is inadequate as it is hard to handle by a normal mechanical workshop and the latter has a relatively high magnetic susceptibility which is detrimental in the environment of strong magnetic fields as it is the case in the ion microscope experiment. Titanium turned out to be a reasonable choice as it has a very weak magnetic susceptibility and at the same time a linear thermal expansion coefficient  $\alpha_L \approx 8.41 \cdot 10^{-6}/\text{K}$  which is still by a factor of two smaller than most of the common stainless steels and by factor 2.8 smaller than aluminium [32].

In order to examine temperature dependent position shifts of the lattice a 24-hour measurement was done for which the Raspberry Pi was programmed to take one picture each minute. A thermometer was positioned right next to the titanium mount on the side of the quarter-waveplate likewise taking temperature data once a minute. The measurement was started at about 1:40 pm and stopped at the same time on the next day. As shown in figure 4.10, the temperature starts at a value of 21.8 °C (a consequence of holding the thermometer in hands), increases during the afternoon and drops uniformly in the night-time hours to rise again after 14 hours of measurement.

The local maximum after 4.5 hours has a value of 21.5 °C and the minimum after 13 hours amounts to 19.9 °C. This means that the maximum temperature span which was entirely recorded adds up to  $\Delta T = 1.6 \text{ K}$ . To evaluate the lattice's position shift, the taken images were cut to size of the relevant region of the light spot and the same pixel row was extracted from each picture and written into a new matrix  $A$ . As each row of  $A$  depicts the lattice at a certain point of time, the position shift over time can be visualised by plotting the matrix using a color code for the values of brightness given by the individual pixels (see figure 4.11).

As a first remark it may be stated that the laser intensity varies significantly during the measurement leading to brighter and darker sequences from top to bottom of the graph. As a side effect, the visibility increases for lower light intensity which is marked by sharp horizontal lines within the picture. However, the intensity fluctuations remain within the acceptable margins which were determined in chapter 4.3.2 and therefore do not warp the results.

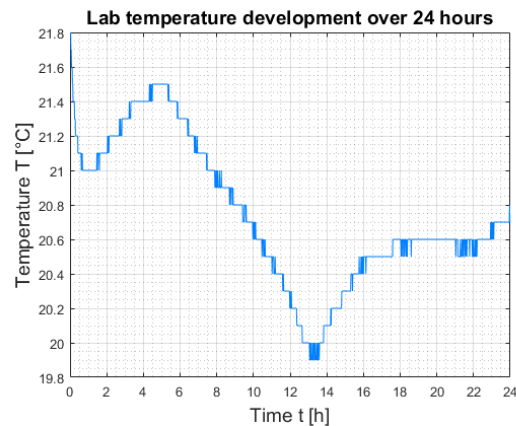


**Figure 4.10.:** Temperature evolution next to the experimental setup over a time span of 24 hours. The temperature value drops from a local maximum of 21.5 °C to a minimum of 19.9 °C within 9 hours during the night.

Figure 4.12 shows an excerpt of fig. 4.11 that demonstrates the position shift in a more distinct way. By following the yellow lines that mark the intensity maxima and comparing them with neighbouring peaks one can already tell that the phase shift causing the position shift exceeds a value of  $2\pi$  between maximal displacements.

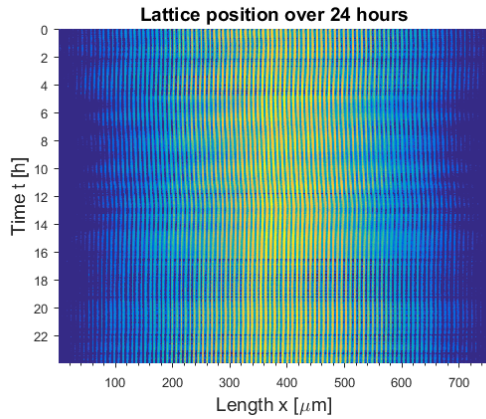


**Figure 4.11.:** Time evolution of lattice position composed of the same extracted pixel row of each image that was taken during the 24-hour measurement.

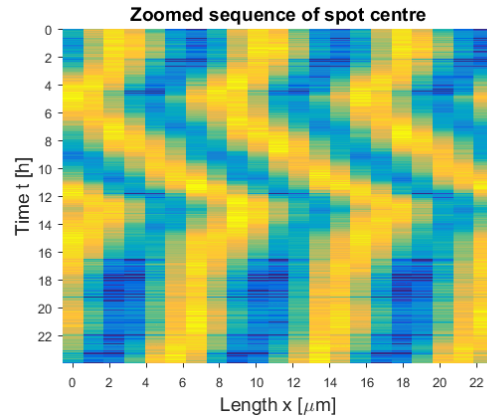


**Figure 4.12.:** Time evolution from fig. 4.11 confined to 21 pixels of the spot centre to illustrate the lattice's position shift over 24 hours. The position varies over more than  $2\pi$ .

The shape of the position shift in fig. 4.12 indicates a strong correlation with the temperature curve in fig. 4.10. By tracking the yellow maximum stripes one can translate the image sequence into absolute lattice shifts in positive or negative x-direction. Such a plot is given in figure 4.13 along with the temperature curve from fig. 4.10 for straightforward comparability.

It is striking that the green shift curve follows the temperature development almost perfectly. Whenever the temperature increases, a negative lattice shift  $\Delta x$  is detected. The same holds true for the opposite direction which can clearly be seen at the enduring temperature drop between hours 5 and 13.  $\Delta x$  is slightly shifted to the right compared to  $T$  and doesn't resolve every single temperature which is due to the finite time that it takes for the material to heat up/ cool down and expand. The lattice period used for the 24-hour measurement was  $i = 7 \mu\text{m}$ . From the temperature development and the lattice shift displayed in figure 4.11, the temperature drift that causes a lattice shift by  $\pi$  is calculated to be  $\Delta T(\pi) = 0.63 \text{ K}$ . Translated into the lattice shift for 1 K temperature drift, this gives a thermal stability of  $1.59 \times \pi \text{ rad/K}$ .

A rough test is conducted to find out whether the assumed linear expansion coefficient of titanium matches the experimental results. Therefore, equation (2.18) is rearranged to the form

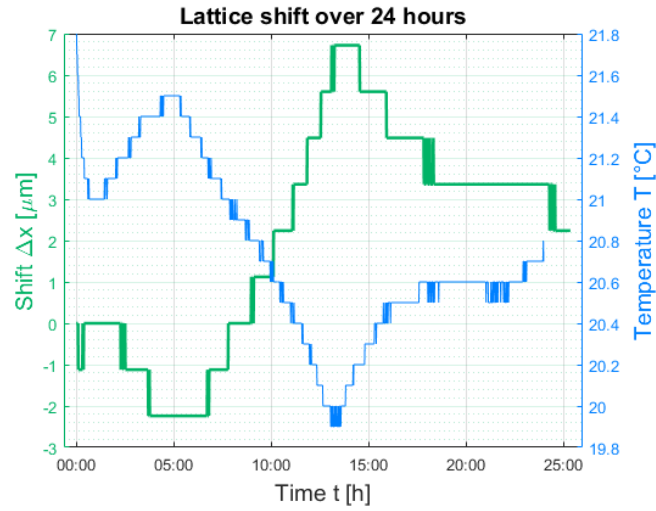


**Figure 4.13.:** Lattice shift and temperature development over 24h. The lattice shift (green line) follows the temperature development.

$$L = \frac{1}{\alpha_L} \cdot \frac{\Delta L}{\Delta T}.$$

Plugging in the values  $\alpha_L = 8.6 \cdot 10^{-6}$  (1/K),  $\Delta L = (1020/2) \cdot 10^{-9}$  m and  $\Delta T = 0.63$  K gives a length of  $L \approx 94$  mm. This quantity describes twice the distance between the first PBS and the reflecting mirror behind the quarter-wave plate (see. 3.1) where the two beams take different paths. The real value of this distance is hard to measure but both the order of magnitude and the approximate value are consistent with the calculated figure.

## 5. Summary

This thesis reports on the design and the setup of an optical accordion lattice for the purpose of calibrating an ion microscope in an ultracold Rydberg experiment. To this end, the lattice will be used to photoionise atoms in a well-defined spatial pattern.

The setup is based on the schematic concept given by Li et al. [31] and was further developed to feature a particularly compact and modular design. It is customised to meet a variety of experimental requirements and to fit into the existing architecture of the ion microscope experiment. The design features optical access for additional cooling and Rydberg excitation lasers. Furthermore, it enables the housing of the central setup unit and offers space to apply Peltier elements and temperature sensors for enhanced thermal stability.

For both thermal and mechanical stability, the design was kept as monolithic as possible and titanium was selected as the mount material. Titanium is characterised by a comparably small coefficient of linear thermal expansion and is suitable for applications in the environment of strong magnetic fields due to its nonmagnetic nature.

The optical accordion lattice is created by two parallel laser beams with a wavelength of 1020 nm which are focused by an aspheric lens and cross in the focal point. A variation of the beam distance in front of the lens changes the crossing angle and thereby the lattice period. To investigate the properties of the optical lattice, a camera was positioned at the focal plane of the lens.

Characterisation was done with respect to the effective range of the lattice period and the interference profile transverse to the optical axis. Furthermore, both the shape of the pattern at off-focal positions and the thermal stability of the setup was examined.

It was ascertained that the lattice period can be varied in the range between 3 and 7  $\mu\text{m}$  where the lower limit is given by the camera resolution and is hence not identical with the physical limit which is expected to lie slightly above 2  $\mu\text{m}$ . The achieved tuning range for the lattice period is well suited for the calibration of the ion microscope and enables a conservative testing of its resolution.

Analysis of the Gaussian lattice profile in the intersection plane of the two beams resulted in approximate lateral lattice extents of  $\Delta x = 215 \mu\text{m}$  and  $\Delta y = 181 \mu\text{m}$ . These are adequate dimensions for ionising an ultracold atomic cloud with a diameter of approximately 100  $\mu\text{m}$ . It could be shown that the visibility of the interference pattern remains above 70 % throughout the whole transverse width of the lattice.

Observation of the lattice pattern in front and behind the crossing point of the two beams led to the conclusion that within a distance of at least  $\pm 3 \text{ mm}$  from the intersection point, the lattice structure remains well-defined in the vicinity of the symmetry plane. In these cases, the extent of

the lattice structure is limited by the regions where the single beam profiles dominate over the interference pattern.

The passive approach to thermal stability by an appropriate selection of the mount material proved to be sufficient for the planned calibration measurements and the resolution testing. A 24-hour measurement showed that the thermally induced lattice shift equals  $1.59 \times \pi$  rad/K.

In case the optical accordion lattice will be used in measurements spanning several hours or even days, the setup needs to be adjusted accordingly. For these purposes, the foundation for active temperature control has been laid.

## 6. Outlook

This thesis has laid the foundation for the use of an optical accordion lattice to calibrate an ion microscope in an ultracold Rydberg experiment and to test its resolution. This chapter comprises several ideas for small further improvements and gives inspiration for different application purposes along with the according adaptations that might be necessary.

In contrast to the work by Li et al. [31], the setup of this thesis lacks the possibility to adjust the mirror behind the quarter-wave plate (see. figure 3.1). As a consequence, the precise alignment of the PBS cubes is no longer irrelevant but crucial for the position of the crossing point of the two beams which forms the lattice. In the case of misalignment, this crossing point will shift when changing the lattice period. An adjustment by bare hands will most probably not lead to a sufficient degree of precision and makes it necessary to compensate intersection shifts by re-adjusting the lens position. This inconvenience gives an incentive to design an appropriate alignment tool.

In the framework of this thesis, it was also considered to create magnified images of the optical lattice. This would enable the study of small lattice periods which is currently limited by the resolution of the camera. The attempts to realise such an imaging system have been limited by the timeframe of this work. Nevertheless, imaging was carried out with different lens systems and resulting magnification factors. In all the tested cases, disturbing interference patterns were observed which hampered further processing of the obtained data. The question about the origin of these interferences could not be answered ultimately but there are strong indications that the cameras ('Pixelfly usb' by pco. and 'Laser Beam Profiler' by Newport) can be hold accountable for these effects.

In the current configuration, the setup can be operated for the calibration and resolution testing purposes that motivated this work. For possible future long-term measurements, spanning hours or even days, the passive thermal stability of titanium might not be sufficient. To improve the stability, the present setup can be modified in the following two manners.

- **Enhanced passive stability by insulating housing:** The titanium setup features several screw holes which can be used to mount a housing for the box. The selected material could be e.g. polystyrene which would shield the setup from both dust and temperature changes of the environment. However, the improvement by this technique might still be dissatisfying as the cladding cannot protect the setup from long-term temperature drifts.

- **Active stabilisation with Peltier elements:** A more promising method to counteract thermally induced lattice shifts is given by an active stabilisation of the temperature inside the mount material with the help of Peltier elements. At both sides of the setup along the critical section between the first cube and the back-reflecting mirror behind the quarter-wave plate, there is space left to apply Peltier elements. These components are driven electrically and can be used to temperature stabilize the whole titanium mount. To be able to control the temperature inside the material, temperature sensors can be inserted in the holes that are dedicated to this purpose (see fig. 3.2).

Another adaptation that would allow an automated operation of the optical accordion lattice with continuous spacing variation can be achieved by a replacement of the manual translation stage by a motorised version.

Although this was not the motivation for this thesis, the setup design at hand can be adapted to trap atoms in the accordion lattice, if a slightly larger wavelength, e.g. 1070 nm, is used. This would open the door to Rydberg experiments in an optical lattice. Such experiments are of extraordinary interest because the length scale of several Rydberg quantities like the binding length of Rydberg molecules [10] or the Rydberg blockade radius [36] match the optical lattice spacings which are achievable in the built setup.

# Appendix

## A. Technical drawings

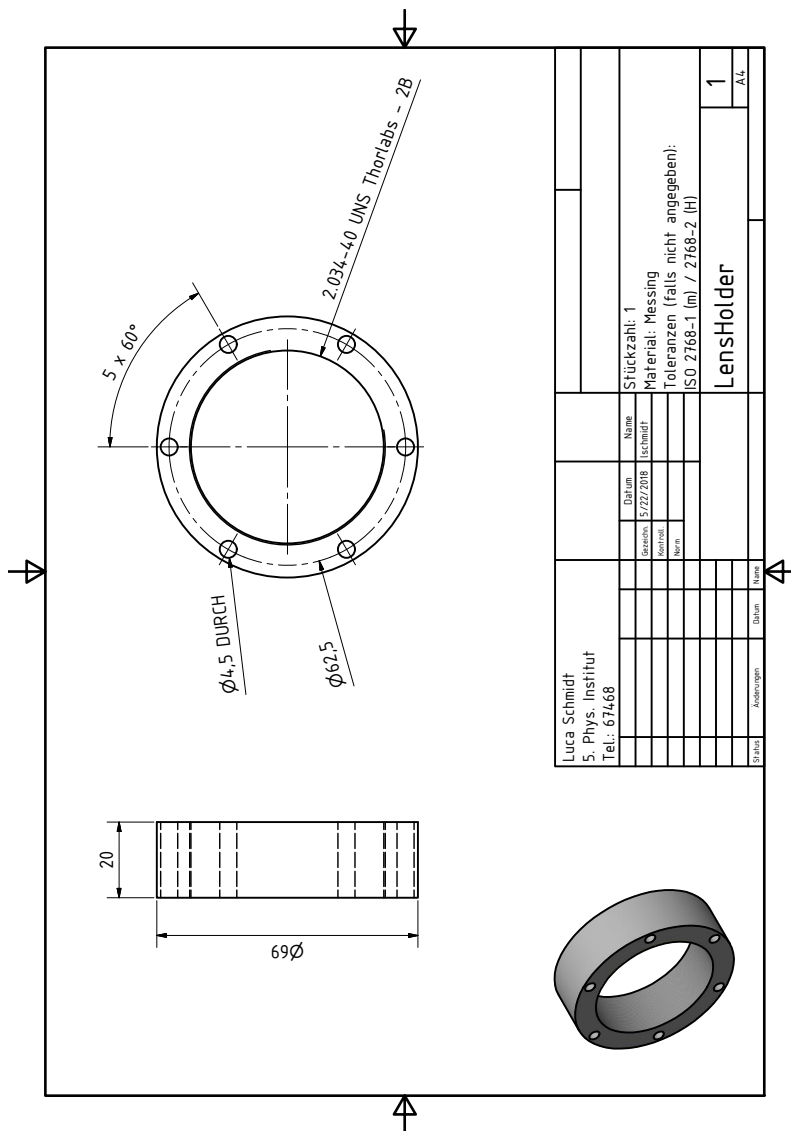


Figure A.1.: Technical drawing of the mount adapter for the aspheric lens.



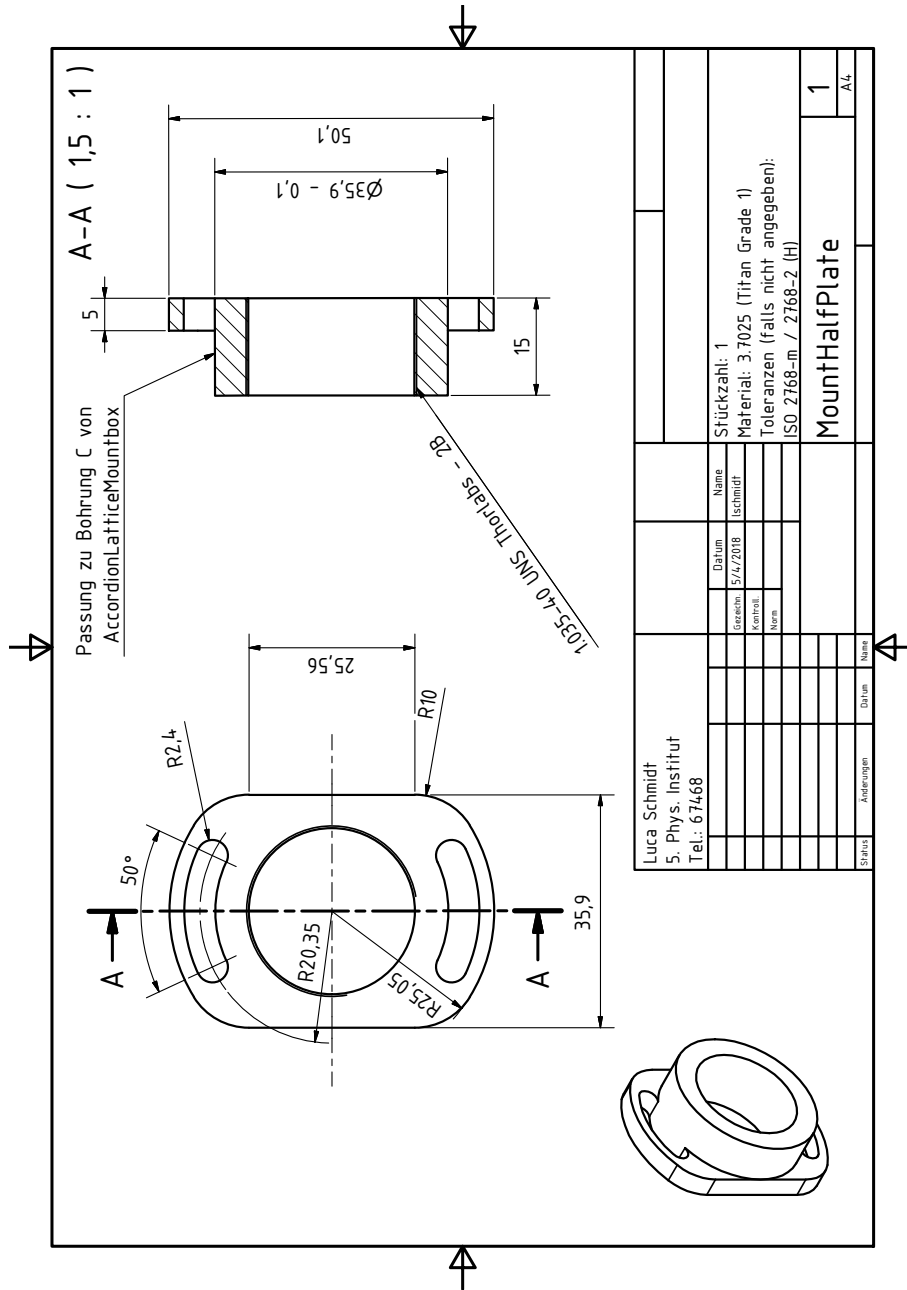


Figure A.3.: Technical drawing of the mount for the half-wave plate.







# List of Figures

1.1.	Level scheme for the photo-ionisation of rubidium atoms to generate a tunable test pattern of ions with an optical accordion lattice (orange stripes, lattice periode $i$ ). The resulting test structure can be used to calibrate and test an ion microscope.	3
1.2.	Sectional drawing of the ion microscope to be calibrated and tested. The tunable ion test pattern will be prepared at the position where later the ultracold atomic cloud will be situated.	3
2.1.	Basic laser components. The pump delivers energy to create a population inversion inside the active medium. Most of the stimulated laser light is reflected between the resonator mirrors and contributes to amplification. A small part of it leaves the resonator via the partly transmissive mirror.	5
2.2.	Energy scheme of a four-level system with ground state, short-lived pump level, long-lived upper laser level and short-lived lower laser level. A population inversion is created between level 0 and level 2 in order to achieve laser operation. Figure taken from [26]	5
2.3.	Energy-momentum relation for electrons in the valence and conduction band of a semiconductor material. Excitation and decay from one band to the other is identified with an absorption and emission of a photon, respectively. Transitions occur at a single wavenumber as the photon's momentum is small compared to the electron's one and thus can be neglected. Figure taken from [27].	6
2.4.	Beam path inside a telescope consisting of two lenses with focal length $f_1$ and $f_2$ in a distance of $f_1 + f_2$ .	9
2.5.	Setup for imaging an object with a larger scale than the real proportions. Object distance $g$ needs to be greater than image distance $b$ while the distance of the two lenses is arbitrary.	10
2.6.	Spherical aberration due to different focal planes of centre and off-centre rays.[28]	10
2.7.	Phase differences between x- and y-component of the electric field and the resulting polarisation over the range of $2\pi$ [28].	11
2.8.	Development of the Gaussian beam radius $w(z)$ in front and behind the smallest value $w_0$ . The Rayleigh length $z_R$ is given by the distance from the waist position where the beam radius has a value of $\sqrt{2}w_0$ [28].	12

2.9.	Intensity distribution along $r$ at a fixed position $z$ . The width of a Gaussian beam can be defined by the position $r$ where the intensity has dropped to $I_0/e^2$ . $I_0$ defines the maximal intensity in the beam centre [28]. . . . .	12
2.10.	Two laser beams intersecting under an angle $\theta$ after passing a lens. The intersection point is defined to be at the position $y = 0$ . . . . .	15
3.1.	Schematic setup to create an optical accordion lattice which is imaged by a camera in the focal plane of an aspheric lens. The beams in front of an aspheric lens are aligned parallel by two PBS and a quarter-wave plate. Equal intensities of the two beams can be obtained by the use of a half-wave plate before the incident laser beam reaches the cubes. Variation of the beam distance in front of the aspheric lens and thus a tuning of the lattice period is realised via a translation stage that shifts the beam's point of impact on the cubes. . . . .	18
3.2.	Conceptual setup design. . . . .	21
3.3.	Pictures of the manufactured titanium components to mount the half-wave and quarter-wave plates and the assembled titanium setup mounted on the 5-axis-stage. . . . .	21
3.4.	Conceptual setup design integrated in the current environment of the ion microscope experiment. Behind the central setup unit one can see a sectional drawing of the science chamber. . . . .	22
4.1.	Simulated beam path from fibre outcoupler to the focal position after the aspheric lens. . . . .	24
4.2.	Brightness values of the camera pixels for increasing laser intensities. The beam intensity was calculated from power data that was measured in front of the camera sensor. Maximum brightness is associated with the highest brightness values in the pictures and mean brightness refers to the mean values of 16 pixels surrounding the highest data point. For this characterisation, half of the beam was blocked after it was split up by the PBS. . . . .	26
4.3.	Anticipated (blue curve) and measured (asterisked) lattice periods at varying stage positions $d$ . The measurement was limited by the PBS edges for large spacing and the camera resolution in the region of small spacing. . . . .	27
4.4.	Image of the lattice spot that was taken by the Raspberry Pi Camera (left) and extracted horizontal line of the spot centre (right). . . . .	28

4.5.	Analysis of the spot centre line in figure 4.4 (right). The upper plot shows the brightness data as well as maxima and minima values as a guide to the eye. In the bottom plot the maxima values were fitted by a Gaussian function (see. eq.(4.1)) to give an envelope for the brightness data. . . . .	29
4.6.	Analysis of the vertical beam spot profile. The brightness values of the spot image in fig. 4.4 (left) were totalised in horizontal direction and plotted over the vertical length. The displayed fitfunction has a Gaussian shape according to eq.(4.1). . .	30
4.7.	Visibility along the central line of the spot in fig 4.4. It was calculated by using equation (2.17) and taking neighbouring maxima and minima. . . . .	31
4.8.	Lattice images for different positions of the camera along z-direction. Image a) displays an offset of $\Delta z = -3$ mm, b) shows the approximate position where the two beams intersect and c) is the image for $\Delta z = +3$ mm. . . . .	32
4.9.	Lattice profiles for three different positions of the camera along z-direction. . .	32
4.10.	Temperature evolution next to the experimental setup over a time span of 24 hours. The temperature value drops from a local maximum of $21.5^\circ\text{C}$ to a minimum of $19.9^\circ\text{C}$ within 9 hours during the night. . . . .	34
4.11.	Time evolution of lattice position composed of the same extracted pixel row of each image that was taken during the 24-hour measurement. . . . .	35
4.12.	Time evolution from fig. 4.11 confined to 21 pixels of the spot centre to illustrate the lattice's position shift over 24 hours. The position varies over more than $2\pi$ . . . . .	35
4.13.	Lattice shift and temperature development over 24h. The lattice shift (green line) follows the temperature development. . . . .	36
A.1.	Technical drawing of the mount adapter for the aspheric lens. . . . .	41
A.2.	Technical drawing of titanium mount box. . . . .	42
A.3.	Technical drawing of the mount for the half-wave plate. . . . .	43
A.4.	Technical drawing of the mount for the quarter-wave plate and the back-reflecting mirror. . . . .	44
A.5.	Technical drawing of the mount for the elliptical mirror. . . . .	45
A.6.	Technical drawing of the ground plate on which the setup was mounted. . . . .	46

## Bibliography

- [1] J. V. Prodan, W. D. Phillips, and H. Metcalf, “Laser Production of a Very Slow Monoenergetic Atomic Beam,” *Physical Review Letters*, vol. 49, no. 16, pp. 1149–1153, 1982.
- [2] Lett, Watts, Westbrook, Phillips, Gould, and Metcalf, “Observation of atoms laser cooled below the Doppler limit,” *Physical review letters*, vol. 61, no. 2, pp. 169–172, 1988.
- [3] B. Bederson and H. Walther, *Advances in atomic, molecular and optical physics. Vol.37*. San Diego, Calif. and London: Academic Press, 1996.
- [4] Lawall, Bardou, Saubamea, Shimizu, Leduc, Aspect, and Cohen-Tannoudji, “Two-dimensional subrecoil laser cooling,” *Physical review letters*, vol. 73, no. 14, pp. 1915–1918, 1994.
- [5] Lawall, Kulin, Saubamea, Bigelow, Leduc, and Cohen-Tannoudji, “Three-Dimensional Laser Cooling of Helium Beyond the Single-Photon Recoil Limit,” *Physical review letters*, vol. 75, no. 23, pp. 4194–4197, 1995.
- [6] C. J. Foot, *Atomic physics*. Oxford master series in atomic, optical and laser physics, Oxford: Oxford University Press, 2005.
- [7] R. Löw, H. Weimer, J. Nipper, J. B. Balewski, B. Butscher, H. P. Büchler, and T. Pfau, “An experimental and theoretical guide to strongly interacting Rydberg gases,” *Journal of Physics B: Atomic, Molecular and Optical Physics*, vol. 45, no. 11, p. 113001, 2012.
- [8] T. Gallagher, *Rydberg atoms*. Cambridge: Cambridge University Press, 1994.
- [9] Greene, Dickinson, and Sadeghpour, “Creation of polar and nonpolar ultra-long-range rydberg molecules,” *Physical review letters*, vol. 85, no. 12, pp. 2458–2461, 2000.
- [10] V. Bendkowsky, B. Butscher, J. Nipper, J. P. Shaffer, R. Löw, and T. Pfau, “Observation of ultralong-range Rydberg molecules,” *Nature*, vol. 458, pp. 1005 EP –, 2009.
- [11] M. D. Lukin, M. Fleischhauer, R. Cote, L. M. Duan, D. Jaksch, J. I. Cirac, and P. Zoller, “Dipole blockade and quantum information processing in mesoscopic atomic ensembles,” *Physical review letters*, vol. 87, no. 3, p. 037901, 2001.
- [12] K. Singer, M. Reetz-Lamour, T. Amthor, L. G. Marcassa, and M. Weidemüller, “Suppression of excitation and spectral broadening induced by interactions in a cold gas of Rydberg atoms,” *Physical review letters*, vol. 93, no. 16, p. 163001, 2004.

- 
- [13] T. Peyronel, O. Firstenberg, Q.-Y. Liang, S. Hofferberth, A. V. Gorshkov, T. Pohl, M. D. Lukin, and V. Vuletić, “Quantum nonlinear optics with single photons enabled by strongly interacting atoms,” *Nature*, vol. 488, pp. 57 EP –, 2012.
- [14] H. Labuhn, D. Barredo, S. Ravets, S. de Léséleuc, T. Macrì, T. Lahaye, and A. Browaeys, “Tunable two-dimensional arrays of single Rydberg atoms for realizing quantum Ising models,” *Nature*, vol. 534, pp. 667 EP –, 2016.
- [15] H. Bernien, S. Schwartz, A. Keesling, H. Levine, A. Omran, H. Pichler, S. Choi, A. S. Zibrov, M. Endres, M. Greiner, V. Vuletić, and M. D. Lukin, “Probing many-body dynamics on a 51-atom quantum simulator,” *Nature*, vol. 551, no. 7682, pp. 579–584, 2017.
- [16] A. Gaëtan, Y. Miroshnychenko, T. Wilk, A. Chotia, M. Viteau, D. Comparat, P. Pillet, A. Browaeys, and P. Grangier, “Observation of collective excitation of two individual atoms in the Rydberg blockade regime,” *Nature Physics*, vol. 5, pp. 115 EP –, 2009.
- [17] M. Saffman, T. G. Walker, and K. Mølmer, “Quantum information with Rydberg atoms,” *Reviews of Modern Physics*, vol. 82, no. 3, pp. 2313–2363, 2010.
- [18] E. Urban, T. A. Johnson, T. Henage, L. Isenhower, D. D. Yavuz, T. G. Walker, and M. Saffman, “Observation of Rydberg blockade between two atoms,” *Nature Physics*, vol. 5, pp. 110 EP –, 2009.
- [19] L. Béguin, A. Vernier, R. Chicireanu, T. Lahaye, and A. Browaeys, “Direct measurement of the van der Waals interaction between two Rydberg atoms,” *Physical review letters*, vol. 110, no. 26, p. 263201, 2013.
- [20] G. Günter, H. Schempp, M. Robert-de Saint-Vincent, V. Gavryusev, S. Helmrich, C. S. Hofmann, S. Whitlock, and M. Weidemüller, “Observing the dynamics of dipole-mediated energy transport by interaction-enhanced imaging,” *Science (New York, N.Y.)*, vol. 342, no. 6161, pp. 954–956, 2013.
- [21] A. Schwarzkopf, R. E. Sapiro, and G. Raithel, “Imaging spatial correlations of Rydberg excitations in cold atom clouds,” *Physical review letters*, vol. 107, no. 10, p. 103001, 2011.
- [22] I. W. Drummond, “The ion optics of low-energy ion beams,” *Vacuum*, vol. 34, no. 1-2, pp. 51–61, 1984.
- [23] Markus Stecker, Hannah Schefzyk, József Fortágh, and Andreas Günther, “A high resolution ion microscope for cold atoms,” *New Journal of Physics*, vol. 19, no. 4, p. 043020, 2017.
- [24] H. Dinesch, “Entwicklung eines hochauflösenden Ionenmikroskops für kalte Atome.”

- 
- [25] T. Schmid, C. Veit, N. Zuber, R. Löw, T. Pfau, M. Tarana, and M. Tomza, “Rydberg Molecules for Ion-Atom Scattering in the Ultracold Regime,” *Physical review letters*, vol. 120, no. 15, p. 153401, 2018.
- [26] Marius Plach, *Setup of a frequency-doubled high-power laser system in the blue for Rydberg atom spectroscopy*. Bachelor Thesis, Universität Stuttgart, Stuttgart, 03/06/2018.
- [27] R. Diehl, *High-power diode lasers: Fundamentals, technology, applications / Roland Diehl (ed.) ; with contributions by numerous experts*, vol. v.78 of *Topics in applied physics*. Berlin and London: Springer, 2000.
- [28] E. Hecht, *Optics*. Boston: Pearson, 5th ed. ed., op. 2017.
- [29] B. E. A. Saleh and M. C. Teich, *Fundamentals of photonics*. 1991.
- [30] D. A. Steck, *Classical and Modern Optics*.
- [31] T. C. Li, H. Kelkar, D. Medellin, and M. G. Raizen, “Real-time control of the periodicity of a standing wave: an optical accordion,” *Optics Express*, vol. 16, no. 8, p. 5465, 2008.
- [32] “CRC handbook of chemistry and physics,” pp. Online–Ressource, 2007.
- [33] R. C. Weast, ed., *Handbook of chemistry and physics: A ready-reference book of chemical and physical data*. Boca Raton, Florida: CRC Press, 64. ed., 2nd pr ed., 1984.
- [34] Carolin Dietrich. private communication, University of Stuttgart.
- [35] SCHOTT AG, “Technical Details of Zerodur.”
- [36] P. Schauß, M. Cheneau, M. Endres, T. Fukuhara, S. Hild, A. Omran, T. Pohl, C. Gross, S. Kuhr, and I. Bloch, “Observation of spatially ordered structures in a two-dimensional Rydberg gas,” *Nature*, vol. 491, pp. 87 EP –, 2012.

# Acknowledgement

When I started to work on this thesis, I had little knowledge about both the topic and the working methods in a physics laboratory. This has changed substantially during the last four months and I owe much of my development to the people who have supported and supervised me throughout the whole period.

At this point, I would like to thank the people that have contributed to my bachelor thesis in a multitude of ways.

- **Prof. Dr. Tilman Pfau** for giving me the chance to write my thesis in one of his research groups as well as for the positive atmosphere at the institute and the enjoyable hiking trip.
- **Thomas Schmid, Christian Veit** and **Nicolas Zuber** for their technical support and knowledge transfer, their exceptional commitment as supervisors and their inexhaustible patience up until the last minute. It was a pleasure to work with you and I really enjoyed being an occasional participant in the Rybli's *Stammtisch*.
- **Christian Tomschitz, Lucas Hofer** and **Carolin Dietrich** for their technical expertise and kindness.
- **Hermann Kahle** for the encouragement to begin my studies in physics and to stay the course.
- **My parents** for their financial and personal support at any time.
- The whole **membership of the PI5** for all the enjoyable, funny and enlightening conversations and social activities.